THE INFRARED NUCLEAR EMISSION OF SEYFERT GALAXIES ON PARSEC SCALES: TESTING THE CLUMPY TORUS MODELS

C. RAMOS ALMEIDA[1], N. A. LEVENSON[2], J. M. RODRÍGUEZ ESPINOSA[1], A. ALONSO-HERRERO[3], A. ASENSIO RAMOS[1],
J. T. RADOMSKI[4], C. PACKHAM[5], R. S. FISHER[6], AND C. M. TELESCO[5]

[1] Instituto de Astrofísica de Canarias (IAC), C/Vía Láctea, s/n, E-38205, La Laguna, Tenerife, Spain; cra@iac.es
[2] Department of Physics and Astronomy, University of Kentucky, Lexington, KY 40506, USA
[3] Instituto de Estructura de la Materia, CSIC, E-28006 Madrid, Spain
[4] Gemini South Observatory, Casilla 603, La Serena, Chile
[5] Astronomy Department, University of Florida, 211 Bryant Space Science Center, P.O. Box 112055, Gainesville, FL 32611-2055, USA
[6] Gemini Observatory, Northern Operations Center, 670 North Aòhoku Place, Hilo, HI 96720, USA
Received 2009 April 3; accepted 2009 June 29; published 2009 August 19

ABSTRACT

We present subarcsecond resolution mid-infrared (mid-IR) photometry in the wavelength range from 8 to 20 μm of 18 Seyfert galaxies, reporting high spatial resolution nuclear fluxes for the entire sample. We construct spectral energy distributions (SEDs) that the active galactic nucleus (AGN) dominates, relatively uncontaminated by starlight, adding near-IR measurements from the literature at similar angular resolution. We find that the IR SEDs of intermediate-type Seyferts are flatter and present higher 10 to 18 μm ratios than those of Seyfert 2 galaxies. We fit the individual SEDs with clumpy dusty torus models using the in-house-developed BayesClumpy tool. We find that the clumpy models reproduce the high spatial resolution measurements. Regardless of the Seyfert type, even with high spatial resolution data, near- to mid-IR SED fitting poorly constrains the radial extent of the torus. For the Seyfert 2 galaxies, we find that edge-on geometries are more probable than face-on views, with a number of clouds along equatorial rays of $N_0 = 5–15$. The 10 μm silicate feature is generally modeled in shallow absorption. For the intermediate-type Seyferts, N_0 and the inclination angle of the torus are lower than those of the Seyfert 2 nuclei, with the silicate feature appearing in weak emission or absent. The columns of material responsible for the X-ray absorption are larger than those inferred from the model fits for most of the galaxies, which is consistent with X-ray absorbing gas being located within the dust sublimation radius, whereas the mid-IR flux arises from an area farther from the accretion disk. The fits yield both the bolometric luminosity of the intrinsic AGN and the torus-integrated luminosity, from which we derive the reprocessing efficiency of the torus. In the models, the outer radial extent of the torus scales with the AGN luminosity, and we find the tori to be confined to scales less than 5 pc.

Key words: galaxies: active – galaxies: nuclei – galaxies: Seyfert – infrared: galaxies

Online-only material: color figures

1. INTRODUCTION

The unified model for active galaxies (Antonucci 1993; Urry & Padovani 1995) explains the observed differences between Type-1 and Type-2 objects as due to orientation. Although the unification model may not be universally applicable, the most accepted scheme is that there is dust surrounding the central region of active galactic nuclei (AGNs) distributed in a toroidal geometry (Pier & Krolik 1993; Granato & Danese 1994; Efstathiou & Rowan-Robinson 1995; Granato et al. 1997). Thus, the central engines of Type-1 AGNs can be seen directly, resulting in typical spectra with both narrow and broad emission lines coming from the narrow-line region (NLR) and the broad-line region (BLR), respectively. In Type-2 AGNs, the active nucleus and the BLR are obscured by an optically and geometrically thick dusty torus, which explains the lack of broad lines in their observed spectra. The torus dust grains absorb ultraviolet photons from the central engine and re-radiate them in the infrared (IR), peaking at mid-IR wavelengths (7–26 μm).

Pioneering work in modeling dusty tori was performed by Pier & Krolik (1992). They assumed a uniform dust density distribution of a few parsecs radial extent. However, in order to better reproduce the observations, Pier & Krolik (1993) enlarged the torus, e.g., to account for the far-IR emission. Thus, the coolest material in the torus must be located far from the central

engine, implying ∼100 pc scale tori. Further investigations with smooth dust distributions were carried out by Granato & Danese (1994), Efstathiou & Rowan-Robinson (1995), Granato et al. (1997), and Siebenmorgen et al. (2004a).

However, recent ground-based mid-IR observations of nearby Seyferts reveal that the torus size is likely restricted to a few parsecs. For example, Packham et al. (2005) and Radomski et al. (2008) established upper limits of 2 and 1.6 pc for the outer radii of the Circinus galaxy and Centaurus A tori, respectively, using data from the Gemini Telescopes. Additionally, interferometric observations obtained with the MID-infrared Interferometric Instrument (MIDI) at the Very Large Telescope Interferometer (VLTI) of Circinus, NGC 1068, and Centaurus A suggest a scenario where the torus emission would only extend out to $R = 1$ pc (Tristram et al. 2007), $R = 1.7–2$ pc (Jaffe et al. 2004; Raban et al. 2009), and $R = 0.3$ pc (Meisenheimer et al. 2007), respectively.

Thus, during the last decade, an intensive search for an alternative geometry to the early homogeneous torus models has been carried out in order to explain the observations. Before Pier & Krolik (1992, 1993) publications, Krolik & Begelman (1988) claimed that smooth dust distributions cannot survive within the AGN vicinity. They proposed that the material in the torus must be distributed in a clumpy structure, in order to prevent the dust grains from being destroyed by the hot surrounding gas.

The first results of radiative transfer calculations of a clumpy medium were reported by Nenkova et al. (2002), and further work was done by Dullemond & van Bemmel (2005), Fritz et al. (2006), Elitzur & Shlosman (2006), and Ballantyne et al. (2006).

Thus, the clumpy dusty torus models (Nenkova et al. 2002, 2008a, 2008b; Hönig et al. 2006; Schartmann et al. 2008) propose that the dust is distributed in clumps, instead of homogeneously filling the torus volume. These models are making significant progress in accounting for the mid-IR emission of AGNs. A fundamental difference between clumpy and smooth density distributions of dust is that the former implies that both directly illuminated and shadowed cloud faces may exist at different distances from the central engine. Thus, the dust temperature is not a function of the radius only, as was the case in the homogeneous models, since illuminated and shadowed clouds contribute to the IR emission from all viewing angles. Homogeneous torus models had serious difficulties in predicting the observed differences in the variety of spectral energy distributions (SEDs; Spinoglio & Malkan 1989; Fadda et al. 1998; Kuraszkiewicz et al. 2003; Alonso-Herrero et al. 2003; Rigby et al. 2004) and the strengths of the 10 μm silicate feature in both Seyfert 1 and Seyfert 2 nuclei (Roche et al. 1991; Granato et al. 1997; Mason et al. 2006), and also the large optical depths along the line of sight indicated by X-ray observations (Simpson et al. 1994; Tozzi et al. 2001). Inhomogeneous torus models solve these problems. The clumpy models have been employed in several observational studies, e.g., the first *Spitzer* analysis of AGN in the GOODS fields (Treister et al. 2004), and in the analysis of the 10 μm spatially resolved spectra of NGC 1068 and NGC 2110 nuclei (Mason et al. 2006, 2009).

Since the reprocessed radiation from the torus is re-emitted in the IR, this range (especially the mid-IR) is key to put constraints on the clumpy dusty torus models. In comparing the predictions of any torus model with observations, the small-scale torus emission must be isolated. Large aperture data (i.e., images with angular resolutions larger than 1–1″.5, such as those provided by *ISO*, *IRAS*, or *Spitzer*) are strongly contaminated with emission from the host galaxy. For example, starburst emission is an important source of IR flux in the majority of AGNs (Netzer et al. 2007; Barmby et al. 2006; Polletta et al. 2007; Ramos Almeida et al. 2009). Mason et al. (2006) found for NGC 1068 that all flux measurements within apertures smaller than 0″.5 were well fitted by the models, whereas larger aperture fluxes were much higher and presented a different spectral shape in the mid-IR. This excess of emission could be due to nearby dust outside the torus, that is also emitting in the IR (see, e.g., Roche et al. 2006). Mason et al. (2006) concluded for NGC 1068 that the torus contributes less than 30% of the 10 μm flux within apertures larger than 1″. The bulk of this large-aperture flux comes from dust in the ionization cone, which occupies a larger volume than the torus dust.

At shorter IR wavelengths ($\sim$1–2.2 μm), the flux contained in apertures of a few arcseconds partly comes from the torus and partly from stellar emission. Alonso-Herrero et al. (1996) found that for Seyfert 2 galaxies (Sy2) the fluxes obtained within a 3″ aperture are dominated by stellar emission in the near-IR, out to $\sim$2 μm. Indeed, Kotilainen et al. (1992) found for a complete sample of Seyfert galaxies, most of them Seyfert 1 (Sy1), that starlight contributes significantly to the nuclear emission in the near-IR (J, H, and K bands), even within a small projected aperture (of 3″). Consequently, high angular resolution observations at these wavelengths are crucial to separate the pure nuclear emission from that of the host galaxy, which contaminates or hides the AGN emission.

The optimal way to estimate near-IR nuclear fluxes uncontaminated by star formation, in as much as possible, is the use of either subarcsecond spatial resolution data (e.g., from the *Hubble Space Telescope* (*HST*) or adaptive optics) or high spatial resolution ground-based data, extracting the nuclear emission in a proper manner (e.g., using point-spread function (PSF) subtraction). In the mid-IR, it is necessary to isolate the torus emission from that produced by dust in the ionization cones or dust heated by intense star formation. With various high-resolution SEDs covering the near- and mid-IR ranges, it is possible to identify SED features that are attributable to the torus.

It is worth mentioning that mid-IR interferometry constitutes the most precise way of characterizing the torus structure using observations and comparing them with the torus models (e.g., Hönig et al. 2006). However, the signal-to-noise ratio (S/N) required for VLTI observations strongly restricts the number of observable sources to the nearest AGN only.

In this work, we report new high-resolution mid-IR imaging data for 18 nearby Seyfert galaxies, for which we have estimated nuclear mid-IR fluxes.[7] We also compiled near-IR high spatial resolution fluxes from the literature to construct pure-nuclear SEDs. We have fitted these AGN SEDs with the clumpy dusty torus models of Nenkova et al. (2008a, 2008b) to constrain the parameters that describe the clumpy models when applied to Seyfert galaxies. Table 1 summarizes key observational properties of the sources in the sample. Section 2 describes the observations, data reduction, and compilation of near-IR fluxes. Section 3 presents the main observational results, and Section 4 presents the modeling results. We draw conclusions about the clumpy torus models and AGN obscuration in general in Section 5. Finally, Section 6 summarizes the main conclusions of this work.

2. OBSERVATIONS AND DATA REDUCTION

2.1. Mid-IR Imaging Observations

Ground-based mid-IR high angular resolution observations of 18 nearby active galaxies were carried out over the past years for a variety of science drivers. We make use of this archive of data in this paper. Most of these sources are Type-2 Seyferts, but the sample also includes two Seyfert 1.9 (Sy1.9), one Seyfert 1.8 (Sy1.8), two Seyfert 1.5 (Sy1.5), and one Sy1 galaxy (see Table 1).

The first set of observations was obtained with the University of Florida mid-IR camera/spectrometer OSCIR, in 1998 December at the 4 m Blanco Telescope at Cerro Tololo Inter-American Observatory (CTIO) and in 2001 May at the Gemini-North Telescope. This instrument employs a Rockwell 128 × 128 pixel Si:As blocked impurity band (BIB) detector array, optimized for the wavelength range between 8 and 25 μm. On CTIO, the pixel scale is 0″.183, with a field of view (FOV) of 23″.4 × 23″.4, and the resolutions obtained were $\sim$1″ at both 10.7 and 18.2 μm. On Gemini North, OSCIR has a plate scale of 0″.089 pixel^{-1} and a total FOV of 11″ × 11″. The achieved resolutions were $\sim$0″.5 at 10.7 μm and $\sim$0″.6 at 18.2 μm. Another set of observations was performed with the mid-IR camera/spectrograph

---

[7] The mid-IR images of Circinus, NGC 4151, and Centaurus A are already published by Packham et al. (2005) and Radomski et al. (2003, 2008), respectively. However, we present new calculations of the nuclear mid-IR fluxes in this work.

Table 1
Basic Galaxy Data

Galaxy	Seyfert Type	Morphology	z	Distance (Mpc)	Scale (pc arcsec^{-1})
Centaurus A	Sy2	S0 pec	0.0018	3.5[a]	17
Circinus	Sy2	SA(s)b:	0.0014	4[a]	20
IC 5063	Sy2	SA(s)0+:	0.0113	45	219
Mrk 573	Sy2[b]	(R)SAB(rs)0+:	0.0172	69	334
NGC 1386	Sy2	SB(s)0+	0.0029	11[a]	56
NGC 1808	Sy2	(R$'_1$)SAB(s:)b	0.0033	11[a]	64
NGC 3081	Sy2	(R$_1$)SAB(r)0/a	0.0080	32	155
NGC 3281	Sy2	SAB(rs+)a	0.0107	43	208
NGC 4388	Sy2	SA(s)b: sp	0.0084	34	163
NGC 5728	H ɪɪ/Sy2	(R$_1$)SAB(r)a	0.0094	38	182
NGC 7172	H ɪɪ/Sy2	Sa pec sp	0.0087	35	169
NGC 7582	Sy2	(R$'_1$)SB(s)ab	0.0053	21	103
NGC 1365	H ɪɪ/Sy1.8	(R$'$)SBb(s)b	0.0055	18[a]	107
NGC 2992	Sy1.9	Sa pec	0.0077	31	149
NGC 5506	Sy1.9[b]	Sa pec sp	0.0062	25	120
NGC 3227	Sy1.5	SAB(s) pec	0.0039	17[a]	82
NGC 4151	Sy1.5	(R$'$)SAB(rs)ab:	0.0033	13[a]	64
NGC 1566	Sy1	(R$'_1$)SAB(rs)	0.0050	20	97

Notes. Classification, morphological class, and spectroscopic redshift of our targets taken from the NASA/IPAC Extragalactic Database (NED). The distance to the sources and the physical scale have been obtained using $H_0 = 75$ km s^{-1} Mpc^{-1}.
[a] For the cases of the most nearby objects, i.e., Centaurus A, Circinus, NGC 1386, NGC 1808, NGC 1365, NGC 3227, and NGC 4151, the values of the distance to the galaxies have been taken from Radomski et al. (2008), Packham et al. (2005), Bennert et al. (2006), Jiménez-Bailón et al. (2005), Silbermann et al. (1999), Davies et al. (2006), and Radomski et al. (2003), respectively.
[b] Mrk 573 and NGC 5506 have recently been classified as obscured narrow-line Sy1 galaxies (Nagar et al. 2002; Dewangan & Griffiths 2005; Ramos Almeida et al. 2008).

T-ReCS (Thermal-Region Camera Spectrograph; Telesco et al. 1998) on the Gemini-South Telescope. T-ReCS uses a Raytheon 320×240 pixel Si:As IBC array, providing a plate scale of 0$''$089 pixel^{-1}, corresponding to an FOV of 28$''$5 × 21$''$4. The resolutions obtained were 0$''$3–0$''$4 at 8.8 μm, ~0$''$5 at 10.4 μm, and 0$''$5–0$''$6 at 18.3 μm. The last set of observations was made with the mid-IR camera/spectrograph Michelle (Glasse et al. 1997) on the Gemini-North Telescope. The Michelle detector is a Si:As IBC array with a format of 320×240 pixels. Configured in its imaging mode, Michelle has a 0$''$10 pixel^{-1} plate scale, and the resolutions of our observations were ~0$''$4 at 11.3 μm and ~0$''$5 at 18.1 μm. This plate scale translates to an FOV of 32$''$ × 24$''$. A summary of the observations is reported in Table 2.

The standard chopping-nodding technique was used to remove the time-variable sky background, the telescope thermal emission, and the so-called $1/f$ detector noise. The chopping throw was 15$''$, and the telescope was nodded every 30 s. All data were reduced using in-house-developed IDL routines. The difference for each chopped pair for each given nodding set was calculated, and the nod sets were then differenced and combined until a single image was created. Chopped pairs obviously compromised by cirrus, high electronic noise, or other problems were excluded from any further reduction process.

Observations of flux standard stars were made for the flux calibration of each galaxy through the same filters. The uncertainties in the flux calibration were found to be ~5%–10% at the N band and ~15%–20% at the Qa band. PSF star observations were also made immediately prior to or after each galaxy

observation to accurately sample the image quality. These images were employed to determine the unresolved (i.e., nuclear) component of each galaxy. The PSF star, scaled to the peak of the galaxy emission, represents the maximum contribution of the unresolved source, where we integrate flux within an aperture of 2$''$ for the Gemini data, and of 4$''$ for the CTIO data (NGC 1365, NGC 1808, and NGC 7582). The residual of the total emission minus the scaled PSF represents the host galaxy contribution. A detailed study of the extended near nuclear structures of the galaxies in our sample will be the subject of a forthcoming paper (J. T. Radomski et al. 2010, in preparation). We require a flat profile in the residual (for a realistic galaxy profile) and therefore reduce the scale of the PSF from matching the peak of the galaxy emission (100%) to obtain the unresolved fluxes reported in Table 3. Figure 1 shows an example of PSF subtraction at various levels (in contours) for the Sy2 galaxy NGC 4388 in the N$'$ Michelle filter, performed following Radomski et al. (2002) and Soifer et al. (2003). The residual profiles from the different scales demonstrate the best-fitting result, scaled to 90% of the peak flux. The uncertainty in the unresolved fluxes determination from PSF subtraction is ~10%–15%. Thus, we estimated the errors in the flux densities reported in Table 3 by adding quadratically the flux calibration and PSF subtraction uncertainties, resulting in errors of ~15% at the N band and of ~25% at the Qa band.

For the galaxies that clearly appear spatially unresolved in our mid-IR images (Mrk 573, NGC 1566, and NGC 5728), aperture photometry was employed to derive their nuclear density fluxes (reported in Table 3). The rule for their calculation was to ensure that all the unresolved emission was collected in the chosen aperture, with the minimum contribution of foreground contribution as possible. Aperture correction was applied to these fluxes, employing the images of the corresponding standard stars in both N and Qa filters.

2.2. Compilation of Near-IR High Spatial Resolution Data

To construct well-sampled IR SEDs, we compiled near-IR high spatial resolution nuclear fluxes from the literature (reported in Table 4). These fluxes correspond to the observed emission from the nuclear region of the galaxies (unresolved component), with typical spatial scales of the same order as those of our nuclear mid-IR fluxes. NICMOS/*HST* fluxes are available for 10 galaxies, having FWHM for an unresolved PSF ~0$''$13 in the F160W filter and ~0$''$09 in F110W. For the cases of Centaurus A and Circinus, there are also diffraction-limited and near-diffraction-limited adaptive optics NACO/VLT fluxes, respectively. (The FWHM of Centaurus A unresolved component is 0$''$1 in the near-IR bands and for Circinus 0$''$2 in the near-IR bands and <0$''$13 in the L$'$ and M$'$ bands.) We also compiled seeing-limited near-IR nuclear fluxes from the literature, obtained with data from IRCAM3 on the 3.8 m United Kingdom IR Telescope (UKIRT), with NSFCam at the 3 m NASA IRTF telescope, with the IRAC-1 IR array camera on the ESO 2.2 m telescope, and with ISAAC at the 8 m VLT. The angular resolution of these natural seeing-limited images is 0$''$6–0$''$7 in the K band and 0$''$6–0$''$9 in the L band. These ground-based near-IR nuclear fluxes were estimated either using aperture photometry (scaling an annulus of the J-band images to the observed counts in H and K; Simpson 1998; Galliano & Alloin 2008), surface brightness profile deconvolution (Quillen et al. 2001), or PSF scaling (Alonso-Herrero et al. 2001, 2003). Due to the lack of high spatial resolution nuclear fluxes of Seyfert galaxies in the literature, the SEDs in our sample range from very well sampled

Table 2
Summary of Mid-IR Observations

Galaxy	Filters	Instrument	Telescope	Observation Epoch	On-Source Time (s)		PSF FWHM	
					N Band	Q Band	N Band	Q Band
Centaurus A	Si2, Qa	T-ReCS	Gemini S	2004 Jan	2000	1550	0″.30	0″.53
Circinus	Si2, Qa	T-ReCS	Gemini S	2004 Feb	109	109	0″.33	0″.55
IC 5063	Si2, Qa	T-ReCS	Gemini S	2005 Jul	130	304	0″.40	0″.62
Mrk 573	N, Qa	T-ReCS	Gemini S	2003 Dec	217	217	0″.36	0″.54
NGC 1386	N, Qa	T-ReCS	Gemini S	2003 Dec	217	217	0″.31	0″.54
NGC 1808	N, IHW18	OSCIR	CTIO 4m	1998 Dec	300	300	0″.94	1″.02
NGC 3081	Si2, Qa	T-ReCS	Gemini S	2006 Jan	130	304	0″.30	0″.56
NGC 3281	N, Qa	T-ReCS	Gemini S	2004 Jan	260	455	0″.34	0″.58
NGC 4388	N′, Qa	Michelle	Gemini N	2006 May	549	733	0″.34	0″.50
NGC 5728	Si2, Qa	T-ReCS	Gemini S	2005 Jul	130	304	0″.35	0″.56
NGC 7172	N	T-ReCS	Gemini S	2004 May	305	. . .	0″.51	. . .
NGC 7582	N, IHW18	OSCIR	CTIO 4m	1998 Dec	250	250	0″.76	0″.99
NGC 1365	N, IHW18	OSCIR	CTIO 4m	1998 Dec	482	482	0″.92	1″.03
NGC 2992	N′, Qa	Michelle	Gemini N	2006 May	730	1095	0″.32	0″.53
NGC 5506	N′, Qa	Michelle	Gemini N	2006 Apr	546	729	0″.36	0″.51
NGC 3227	N′	Michelle	Gemini N	2006 Apr	300	. . .	0″.39	. . .
NGC 4151	N, IHW18	OSCIR	Gemini N	2001 May	360	480	0″.53	0″.58
NGC 1566	Si2, Qa	T-ReCS	Gemini S	2005 Sep	152	304	0″.30	0″.53

Notes. Images were obtained in the 8.74 μm (Si2, $\Delta\lambda = 0.78$ μm at 50% cut-on/off), 10.36 μm (N, $\Delta\lambda = 5.27$ μm), and 18.33 μm (Qa, $\Delta\lambda = 1.5$ μm) filters with T-ReCS; in the 11.29 μm (N′, $\Delta\lambda = 2.4$ μm) and 18.11 μm (Qa, $\Delta\lambda = 1.9$ μm) filters with Michelle; and in the 10.75 μm (N, $\Delta\lambda = 5.2$ μm) and 18.17 μm (IHW18, $\Delta\lambda = 1.7$ μm) filters with OSCIR.

Table 3
Unresolved Mid-IR Fluxes

Galaxy	Level of PSF Subtraction		Flux Density (mJy)	
	N Band	Qa Band	N Band	Qa Band
Centaurus A	100%	100%	710	2630
Circinus	90%	90%	5620	12790
IC 5063	100%	100%	399	2790
Mrk 573[a]	100%	100%	177	415
NGC 1386	70%	70%	147	457
NGC 1808	40%	60%	227	560
NGC 3081	100%	50%	83	231
NGC 3281	80%	100%	355	1110
NGC 4388	90%	100%	195	803
NGC 5728[a]	100%	100%	25	184
NGC 7172	90%	. . .	68	. . .
NGC 7582	70%	50%	195	527
NGC 1365	90%	100%	321	640
NGC 2992	90%	90%	175	521
NGC 5506	100%	100%	873	2200
NGC 3227	100%	. . .	401	. . .
NGC 4151	90%	100%	1320	3200
NGC 1566[a]	100%	100%	29	117

Notes. The percentages of PSF subtraction level are reported in the employed filters (listed in Table 2). Errors in flux densities are dominated in general by uncertainties in the flux calibration and PSF subtraction (∼15% at the N band and ∼25% at the Qa band).

[a] For the galaxies Mrk 573, NGC 1566, and NGC 5728, aperture photometry was performed with the following aperture radii: 0″.89, 0″.45, and 0″.62, respectively. These fluxes include the corresponding aperture corrections.

SEDs (e.g., Circinus and Mrk 573) to galaxies for which there are no high spatial resolution near-IR nuclear fluxes available (NGC 1566 and NGC 5728).
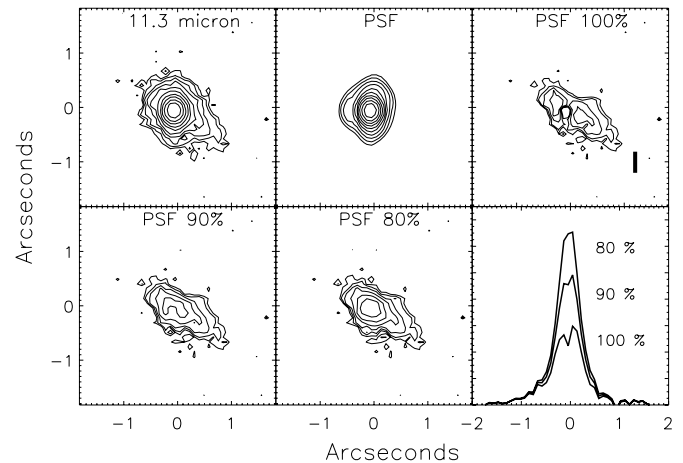

Figure 1. 11.29 μm contour plots of NGC 4388, the PSF star, and the scaled subtraction of the PSF for this galaxy at various levels (100%, 90%, and 80%). The residuals of the subtraction in the lower right panel show the host galaxy profile, with the residual at 90% scale representing the best fit.

3. SED OBSERVATIONAL PROPERTIES

3.1. High Versus Low Spatial Resolution SEDs

Important observational constraints for torus modeling arise from the shape of the IR SEDs of Seyfert galaxies, as the bulk of the torus emission is concentrated in the IR range, peaking at mid-IR wavelengths (7–26 μm). When large aperture data (i.e., of angular resolutions larger than 1–1″.5) such as those from *ISO*, *Spitzer*, or *IRAS*, are employed for constructing SEDs, the IR fluxes are a mixture of AGN plus host galaxy emission. In particular, for the case of Sy2 galaxies, stellar emission dominates the near-IR fluxes at $\lambda \lesssim 2.2$ μm even within 3″ apertures (Alonso-Herrero et al. 1996). Even for Sy1 galaxies, where the direct emission of the AGN is generally the dominant contribution to the near-IR flux, Kotilainen et al.

Table 4
High Spatial Resolution Near-IR Fluxes

Galaxy	Flux Density (mJy)					Filters	Reference(s)
	J Band	H Band	K Band	L Band	M Band		
Centaurus A	1.3 ± 0.1	4.5 ± 0.3	34 ± 2	200 ± 40	· · ·	NACO J,H,K,L	a
Circinus[a]	1.6 ± 0.2	4.8 ± 0.7	19 ± 2	380 ± 38	1900 ± 190	F160W, NACO J,K,L,M	b
IC 5063	· · ·	0.3 ± 0.1	· · ·	· · ·	· · ·	F160W	c
Mrk 573	0.15 ± 0.06	0.54 ± 0.04	3.2 ± 0.6	18.8 ± 3.8	41.3 ± 8.3	F110W,F160W, NSFCam K′,L,M	d
NGC 1386	· · ·	0.2 ± 0.1	· · ·	· · ·	· · ·	F160W	c
NGC 1808	15.5 ± 4.5	· · ·	30.5 ± 8.5	27.5 ± 10.5	· · ·	ISAAC J,Ks,L′	e
NGC 3081	· · ·	0.22 ± 0.13	· · ·	· · ·	· · ·	F160W	c
NGC 3281	· · ·	1.3 ± 0.2	7.7 ± 0.8	103 ± 9	207 ± 25	IRAC-1 H,K, IRCAM3 L′,M	f
NGC 4388	0.06 ± 0.02	0.71 ± 0.28	· · ·	40 ± 8	· · ·	F110W,F160W, NSFCam L	d
NGC 5728	· · ·	· · ·	· · ·	· · ·	· · ·	· · ·	· · ·
NGC 7172	· · ·	<0.4	3.4 ± 0.7	30 ± 6	61 ± 12	IRCAM3 H,K,L′,M	g
NGC 7582	· · ·	22.6 ± 2.3	· · ·	117 ± 18	142 ± 21	F160W, ISAAC L,M	c,h
NGC 1365	· · ·	8.3 ± 0.8	78 ± 8	205 ± 41	177 ± 35	F160W	i
NGC 2992	· · ·	<1	2.8 ± 0.6	22.7 ± 4.5	35.7 ± 7.1	IRCAM3 H,K,L′,M	g
NGC 5506	13.8 ± 2.8	59 ± 12	120 ± 24	340 ± 68	530 ± 106	IRCAM3 J,H,K,L′,M	g
NGC 3227	· · ·	10.6 ± 1.1	22.6 ± 4.5	46.7 ± 9.3	· · ·	F160W, NSFCam K′,L	d
NGC 4151	69 ± 7	104 ± 10	177 ± 35	325 ± 65	449 ± 34	F110W,F160W, NSFCam K′,L, IRCAM3 M	d
NGC 1566	· · ·	· · ·	· · ·	· · ·	· · ·	· · ·	· · ·

Notes. Ground-based instruments and telescopes are: NACO and ISAAC on the 8 m VLT, NSFCam on the 3 m NASA IRTF, IRCAM3 on the 3.8 m UKIRT, and IRAC-1 on the 2.2 m ESO telescope. Measurements in the F110W and F160W filters are from NICMOS on the *HST*.
[a] In the case of Circinus, we also use the 2.42 μm flux (31 ± 3 mJy) from Prieto et al. (2004).
References. (a) Meisenheimer et al. 2007; (b) Prieto et al. 2004; (c) Quillen et al. 2001; (d) Alonso-Herrero et al. 2003; (e) Galliano & Alloin 2008; (f) Simpson 1998; (g) Alonso-Herrero et al. 2001; (h) Prieto et al. 2002; (i) Carollo et al. 2002.

(1992) found that starlight contributes significantly to their nuclear emission. The stellar contribution can also be significant in large-aperture mid-IR measurements. For example, Ramos Almeida et al. (2007) found that the ISOCAM mid-IR fluxes (with an effective resolution in the diffraction limit of ~4″) of a sample of ~60 Seyfert galaxies are dominated by AGN emission in Sy1, although there is a non-negligible contribution from the host galaxy that becomes larger in Sy2.

Using the data described in Section 2, we have constructed high spatial resolution SEDs from ~1 to 18 μm. In order to compare them with large aperture measurements, we have compiled *IRAS* 12 and 25 μm fluxes for the galaxies in our sample, taken from NED (Table 5). We compare the nuclear mid-IR spectral slopes calculated from our N and Q data points (α_{MIR}; Column 3) with the slopes from the *IRAS* 12 and 25 μm measurements (α_{IRAS}; Column 4). If the spectral shape of the *IRAS* SEDs were similar to that of our mid-IR high-spatial resolution data, we would find $\alpha_{MIR} = \alpha_{IRAS}$. However, that is not the case, and except for a couple of galaxies for which both slopes are similar (Mrk 573, NGC 1365, and NGC 1808), the rest of sources are far from the $\alpha_{MIR} = \alpha_{IRAS}$ relationship.

An analogou comparison between our unresolved mid-IR fluxes and the *IRAS* measurements comes from the N/*IRAS* 12 μm and Q/*IRAS* 25 μm ratios (see Table 5). The low values of these ratios indicate the large amount of emission related to stellar processes that is contributing to the *IRAS* fluxes in contrast to our nuclear mid-IR fluxes, that are representative of torus emission. The lowest values of the ratios correspond to Centaurus A, NGC 1365, NGC 1808, NGC 1566, and NGC 7582.

In summary, the high spatial resolution mid-IR measurements provide a spectral shape of the SEDs that is different from that of large aperture data SEDs. The nuclear SEDs presented in this work will allow us to characterize the torus emission and consequently, to use torus models to constrain the distribution of dust in the immediate AGN vicinity.

3.2. Average Seyfert 2 SED

In order to derive general properties of Sy2 galaxies, which constitute the majority of our sample, we constructed an average Sy2 SED, considering only the highest angular resolution data to avoid as much as possible the stellar contamination. This average Sy2 template will be used to compare with the individual SEDs of the Sy2 analyzed in this work, and also with the intermediate-type Seyferts. Out of the 18 galaxies in total (see Table 1), there are 10 "pure" Type-2 Seyferts and two H II/Sy2 composite objects. The rest of the sample consists of other Seyfert types (Sy1.9, Sy1.8, Sy1.5, and Sy1). For constructing the Sy2 average SED, we first excluded the composite objects and the intermediate-type Seyferts. Second, to ensure that we are collecting the best-measured non-stellar nuclear emission, we exclude galaxies with mid-IR data from the 4 m CTIO, because of their lower spatial resolution compared with that of the 8 m Gemini Telescopes. This restriction excludes NGC 1808 and NGC 7582. Indeed, these two galaxies are undergoing intense episodes of nuclear star formation, making it more difficult to isolate the AGN emission from that of the surrounding host galaxy. Finally, in the construction of the average template, we use only *HST* (NICMOS) and VLT (NACO) adaptive optics fluxes in the near-IR. This excludes NGC 3281, for which all the compiled data are ground-based, and a few points in the SEDs of some of the other galaxies (e.g., Mrk 573 and NGC 4388).

Table 5
Spectral Shape Information

Galaxy	α_{IR}	α_{NIR}	α_{MIR}	α_{IRAS}	H/N	N/Q	N/IRAS 12	Q/IRAS 25
Average	3.1 ± 0.9	3.6 ± 0.8	2.0 ± 0.2	. . .	0.003	0.23	. . .	. . .
Centaurus A	2.8 ± 0.8	3.4 ± 0.8	1.8 ± 0.2	0.3 ± 0.1	0.006	0.27	0.03	0.09
Circinus	3.6 ± 1.0	4.5 ± 1.0	1.1 ± 0.1	1.8 ± 0.2	0.001	0.44	0.30	0.19
IC5063	3.8 ± 1.5	4.2 ± 1.7	2.7 ± 0.4	1.8 ± 0.2	0.001	0.14	0.36	0.65
Mrk 573	2.9 ± 0.8	3.4 ± 0.8	1.7 ± 0.1	1.5 ± 0.1	0.003	0.43	0.63	0.49
NGC 1386	3.3 ± 1.2	3.7 ± 1.4	2.0 ± 0.2	1.4 ± 0.1	0.001	0.32	0.28	0.31
NGC 1808	1.8 ± 0.3	1.7 ± 0.2	1.7 ± 0.1	1.6 ± 0.1	. . .	0.41	0.04	0.03
NGC 3081	3.0 ± 1.1	3.5 ± 1.3	1.4 ± 0.1	. . .	0.003	0.36	. . .	. . .
NGC 3281	2.6 ± 0.6	3.1 ± 0.7	2.0 ± 0.2	1.4 ± 0.1	0.004	0.32	0.39	0.42
NGC 4388	3.0 ± 0.8	3.3 ± 0.7	2.7 ± 0.4	1.7 ± 0.2	0.004	0.24	0.19	0.22
NGC 5728	. . .	. . .	2.7 ± 0.2	2.2 ± 0.3	. . .	0.14	0.12	0.18
NGC 7172	1.8 ± 0.2	1.8 ± 0.2	. . .	1.0 ± 0.1	< 0.006	. . .	0.16	. . .
NGC 7582	1.2 ± 0.1	1.1 ± 0.1	1.9 ± 0.1	1.6 ± 0.1	0.116	0.37	0.08	0.07
NGC 1365	1.8 ± 0.4	2.0 ± 0.5	1.3 ± 0.1	1.4 ± 0.1	0.026	0.50	0.06	0.04
NGC 2992	2.4 ± 0.5	2.7 ± 0.4	2.1 ± 0.2	1.0 ± 0.1	< 0.006	0.34	0.24	0.33
NGC 5506	1.7 ± 0.3	2.0 ± 0.3	1.2 ± 0.1	1.6 ± 0.1	0.068	0.40	0.68	0.53
NGC 3227	1.8 ± 0.2	1.8 ± 0.2	. . .	0.9 ± 0.1	0.026	. . .	0.43	. . .
NGC 4151	1.4 ± 0.2	1.3 ± 0.1	1.6 ± 0.1	1.2 ± 0.1	0.079	0.41	0.66	0.66
NGC 1566	. . .	. . .	2.0 ± 0.2	0.6 ± 0.1	. . .	0.25	0.02	0.04

Notes. Fitted spectral indexes ($f_\nu \alpha \nu^{-\alpha}$) in the whole range ($\alpha_{IR}$, from ∼1 to 18 μm), in the near-IR (α_{NIR}, from ∼1 to ∼9 μm), and in the mid-IR (α_{MIR}, using the N and Q band data points). The *IRAS* slopes (α_{IRAS}, determined using the 12 and 25 μm *IRAS* fluxes) are shown also for comparison. H/N and N/Q band ratios are reported, together with the N/12 μm and Q/25 μm *IRAS* ratios.

In the end, we have seven pure Sy2 for constructing the average template: Centaurus A, Circinus, IC 5063, Mrk 573,[8] NGC 1386, NGC 3081, and NGC 4388. Their IR SEDs are shown in Figure 2. We normalize the SEDs at 8.8 μm in order to emphasize the comparison between the N- and both the H- and Q-band data points that provides useful information about the obscuration (see Section 5.1). The measured N/Q ratio for the average template is 0.23 ± 0.14, which is representative of the Sy2 in our sample.

Thus, the average template is constructed with near- and mid-IR data having resolutions ≲0″.6, to ensure the isolation of the torus emission. The best-sampled SED, Circinus, defines the wavelength grid, and we interpolated nearby measurements of the other six galaxies onto this scale. We did not interpolate the sparse observations of IC 5063 and NGC 3081. The interpolated fluxes were used solely for the purpose of deriving the average Sy2 SED template, shown in Figure 2. The error bars correspond to the standard deviation of each averaged point, except for the 8.8 μm point (the wavelength chosen for the normalization). In this case, we assigned a 15% error, the nominal percentage considered for the N-band flux measurements.

3.3. Type-2 Seyfert SEDs

The shape of the Sy2 SEDs in our sample is generally very steep, compared with the intermediate-type Seyferts. In general, Sy2 have steeper 1–10 μm SEDs than Sy1 (Rieke 1978; Edelson et al. 1987; Ward et al. 1987; Fadda et al. 1998; Alonso-Herrero et al. 2001, 2003). Nevertheless, we find a variety of spectral shapes for Sy2, in agreement with Alonso-Herrero et al. (2003).

We measured the 1–18 μm IR slopes ($f_\nu \alpha \nu^{-\alpha_{IR}}$) of the individual Sy2 galaxies and of the average template (Table 5).

The IR slopes are representative of the whole SED shape. We also calculated the near-IR (α_{NIR}, from ∼1 to ∼9 μm) and mid-IR spectral indexes (α_{MIR}, using the N and Q band data points) to compare them. A flat near-IR slope indicates an important contribution of the hot dust emission (up to ∼1000–1200 K; Rieke & Lebofsky 1981; Barvainis 1987) that comes from the inner part of the torus, and consequently, must be hidden in smooth torus descriptions of Sy2.

The Sy2 SEDs are typically steep through the IR, with α_{IR} = 3.1 ± 0.9 for the average template. However, the individual galaxies do show some variety, with α_{IR} ranging from 1.8 to 3.8, being even shallower in the uncertain NGC 7582. Our results are similar to those of Alonso-Herrero et al. (2003), who found α_{IR}^{Alonso} > 2.6 for the 1–16 μm slopes of the Sy2 galaxies in the expanded CfA sample. Comparing the near- and mid-IR slopes for the Sy2 reported in Table 5, we find that $\alpha_{NIR} \gtrsim \alpha_{MIR}$ for all of them, except for NGC 7582. For the average template, α_{NIR} = 3.6 ± 0.8 and α_{MIR} = 2.0 ± 0.2.

The flatter slopes arise naturally in some configurations of clumpy torus models with some near-IR contribution from the hot dust faces of directly illuminated clouds, even when the central engine is blocked from view. In contrast, smooth torus models do not generally produce a range of IR spectral slopes. Indeed, large opacity torus models without extended cone component predict α_{IR} > 4 (Pier & Krolik 1993; Granato & Danese 1994). Homogeneous tori with lower optical depth can flatten the IR slopes (Granato et al. 1997; Fadda et al. 1998), but they predict the 10 μm silicate feature in strong emission for Type-1 nuclei, which is not observed (Roche et al. 1991). The extended conical component included in the Efstathiou & Rowan-Robinson (1995) torus models flattens the 3–5 μm continuum of Sy2. However, the high-resolution measurements considered here should be mostly free of cone contamination. Thus, clumpy dusty torus models seem to be the most promising way for reproducing the observed range of Sy2 SEDs.

[8] Note that Mrk 573 has been recently re-classified by Ramos Almeida et al. (2008) as an obscured NLSy1, but the IR SED remains similar to that of the ordinary Sy2 galaxies.
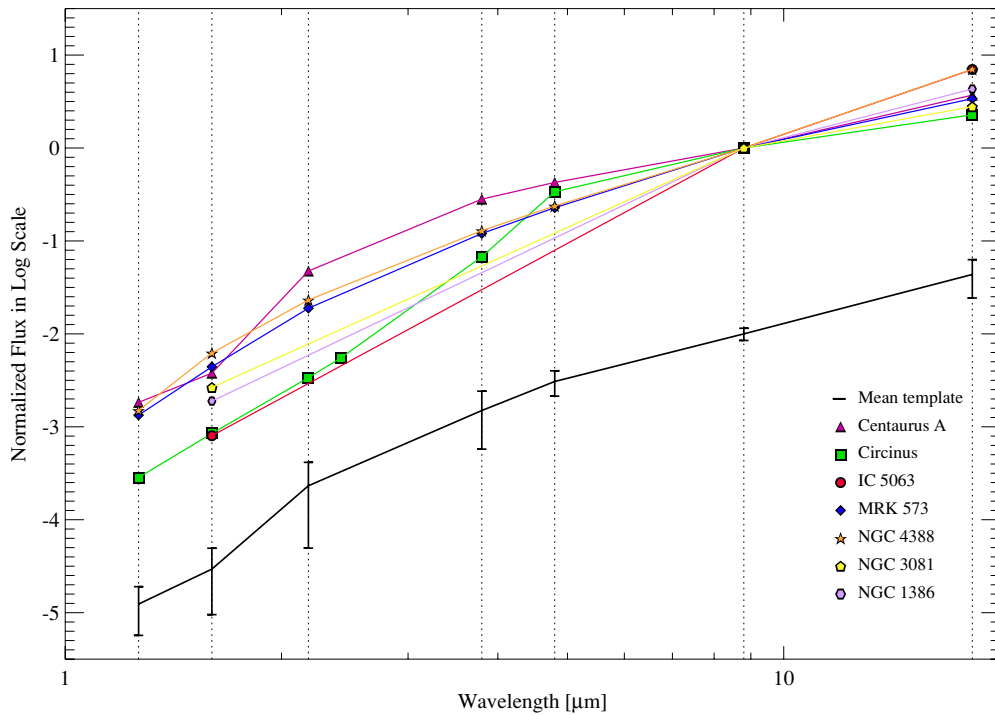
Figure 2. Observed IR SEDs for the seven pure Sy2 galaxies (in color and with different symbols) used for the construction of the average template (solid black). The SEDs have been normalized at 8.8 μm, and the average SED has been shifted in the y-axis for clarity.

(A color version of this figure is available in the online journal.)

3.4. Intermediate-type Seyfert SEDs

The Sy1.5, Sy1.8, and Sy1.9 galaxies were added by Osterbrock (1981) to the Seyfert classification scheme to account for those galaxies with weaker featureless continua, larger broad Balmer decrements, and weaker broad components of the permitted lines than Type-1 Seyferts. Osterbrock (1981) suggested that the observed characteristics of these intermediate Seyferts could be due to the reddening of both the continuum and the BLR by dust. Alonso-Herrero et al. (2003) found for the CfA Seyfert sample that the majority of galaxies optically classified as Sy1.8 and Sy1.9 display either IR spectral indexes and SEDs similar to those of Sy1 or intermediate between Sy1 and Sy2. For the Sy1.5, Alonso-Herrero et al. (2003) found the SEDs to be practically identical to those of Sy1.

Figure 3 shows the SEDs of the five intermediate-type Seyferts considered in this work (two Sy1.5, one Sy1.8, and two Sy1.9), together with the mean Sy2 template for comparison, interpolated onto the mean Sy2 wavelength grid. Spectral indexes are reported in Table 5. The spectral slopes of the intermediate-type Seyferts are shallower than those of the Sy2 (mean slope $\alpha_{\rm IR} = 2.0 \pm 0.4$ for Sy1.8 and Sy1.9 and $\alpha_{\rm IR} = 1.6 \pm 0.3$ for Sy1.5, as opposed to 3.1 ± 0.9). Alonso-Herrero et al. (2003) report IR spectral indices (from 1 to 16 μm) of types 1.8 and 1.9 similar to our measurements ($\alpha_{\rm IR}^{\rm Alonso} = 1.8$–2.6), and within the interval $\alpha_{\rm IR}^{\rm Alonso} = 1.5$–1.6 for Sy1 and Sy1.5 galaxies. The steepest SED among the intermediate-type Seyferts is in the Sy1.9 NGC 2992, which is more similar in shape to the Sy2 SEDs. This result could be due to an incorrect or genuinely changed classification of this galaxy, as Trippe et al. (2008) claim (see the Appendix).

The near-IR slopes of the Sy1.8 and Sy1.9 have intermediate values between those of Sy2 and Sy1.5, with $\alpha_{\rm NIR} > \alpha_{\rm MIR}$. For the Sy1.5 galaxy NGC 4151, $\alpha_{\rm NIR} < \alpha_{\rm MIR}$, indicating the

importance of the hot dust contribution in the SEDs of this type of nucleus.

The H/N and N/Q flux ratios show comparable differences among Seyfert types (Table 5). The H/N ratio is larger for Sy1.5 (0.05 ± 0.04) than for Sy2 (0.003 ± 0.002 for the average template). The N/Q ratios of the intermediate-type Seyferts are also larger than those of Sy2 (mean values of 0.41 ± 0.08 for Sy1.8 and Sy1.9 and 0.41 ± 0.06 for Sy1.5, as opposed to 0.23 ± 0.14).

In summary, the slope of the IR SED is in general correlated with the Seyfert type. Sy2 show steeper SEDs, and intermediate-type Seyferts are flatter. Seyferts 1.8 and 1.9 present intermediate values of the IR slope and H/N ratio between Sy2 and Sy1.5. However, we find a range of spectral shapes among the Sy2 galaxies, and some intermediate-type SEDs have the same slopes as the Sy2. This cannot be reconciled with the predictions of early torus models, since large optical depth homogeneous tori strictly predict steep SEDs for Sy2 and flat SEDs for Sy1. We do not observe such a strong dichotomy (see also Alonso-Herrero et al. 2003). Torus models using lower opacities are observationally discarded (Section 3.3) and models including an extended conical component do not seem adequate for being applied to our high spatial resolution data. Thus, we pursue clumpy torus models of Nenkova et al. (2002) to reproduce the observed SEDs.

4. SED MODELING

4.1. Clumpy Dusty Torus Models

The clumpy dusty torus models of Nenkova et al. (2002, 2008a, 2008b) propose that the dust surrounding the central engine of an AGN is distributed in clumps, instead of homogeneously filling the torus volume. These clumps are distributed with a radial extent characterized by the parameter $Y = R_o/R_d$,
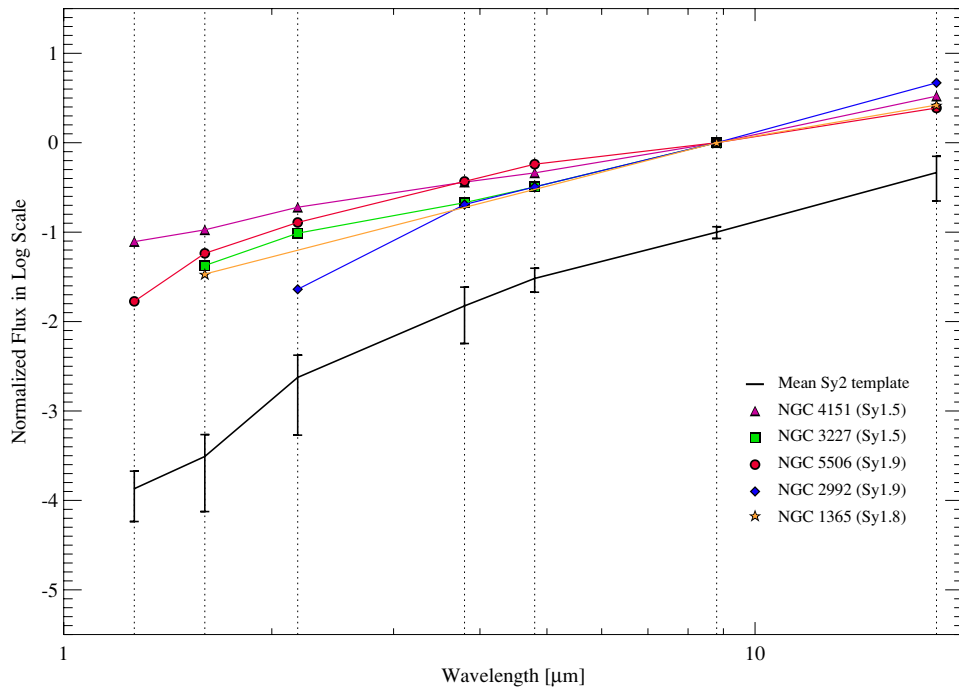
Figure 3. Observed IR SEDs normalized at 8.8 μm for the Sy1.5, Sy1.8, and Sy1.9 galaxies in our sample (in color and different symbols). The average Sy2 SED is displayed for comparison, displaced in the y-axis for clarity. Note the difference in steepness between the Sy2 mean SED and the intermediate types, with the exception of the Sy1.9 NGC 2992.

(A color version of this figure is available in the online journal.)
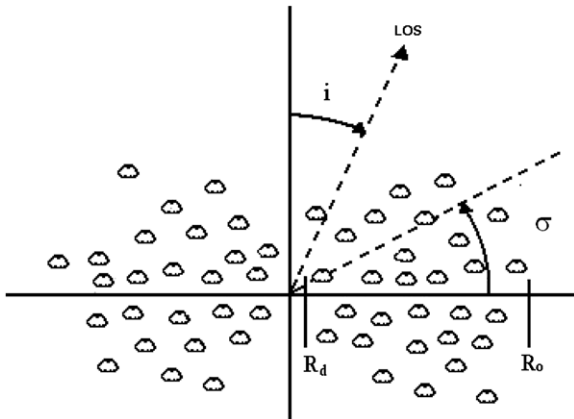

Figure 4. Scheme of the clumpy torus described in Nenkova et al. (2008a, 2008b). The radial extent of the torus is defined by the outer radius (R_o) and the dust sublimation radius (R_d). All the clouds are supposed to have the same τ_V, and σ characterizes the width of the angular distribution. The number of cloud encounters is a function of the viewing angle, i.

where R_o and R_d are the outer and inner radius of the toroidal distribution, respectively (see Figure 4). The inner radius is defined by the dust sublimation temperature ($T_{sub} \approx 1500$ K), with $R_d = 0.4(1500 K T_{sub}^{-1})^{2.6}(L/10^{45} \, \mathrm{erg \, s^{-1}})^{0.5}$ pc. Within this geometry, each clump has the same optical depth (τ_V, defined at V). The average number of clouds along a radial equatorial ray is N_0. The radial density profile is a power law ($\propto r^{-q}$). A width parameter, σ, characterizes the angular distribution, which has a smooth edge. The number of clouds along the line of sight (LOS) at an inclination angle i is $N_{LOS}(i) = N_0 e^{(-(i-90)^2/\sigma^2)}$.

The radiative transfer equations are solved for each clump using the DUSTY code (Ivezić et al. 1999), with solutions depending mainly on the location of each clump within the torus, its optical depth, and the chosen dust composition. We adopt a dust extinction profile corresponding to the OHMc dust (i.e., the standard cold oxygen-rich ISM dust of Ossenkopf et al. 1992). DUSTY includes dust absorption, emission, and scattering components. The total torus emission is calculated by integrating the source function of the whole number of clumps convolved with the radiation propagation probability along the torus (Nenkova et al. 2002). The direct AGN emission may also be included in the resulting SED, which is appropriate for Type-1 nuclei and some intermediate types.

4.2. BayesClumpy

The clumpy database contains $\sim 10^6$ models, calculated for a fine grid of model parameters. The inherent degeneracy between model parameters has to be taken into account when fitting the observables. To this aim, Asensio Ramos & Ramos Almeida (2009) recently developed a Bayesian inference tool (BAYESCLUMPY) that extracts as much information as possible from the observations. They applied interpolation methods that are able to derive models for different combinations of the six clumpy model parameters described above even if they are not present in the original database.

The synthesis code is implemented into a Metropolis–Hastings Markov Chain Monte Carlo algorithm that evaluates the posterior distribution function for the Bayesian inference. This posterior distribution results from taking into account the a priori knowledge about the parameters and the information introduced by the observations. The names and abbreviations of the six parameters that describe the clumpy models, and the intervals considered for the general fitting are detailed in Table 6 (see also Figure 4).

We introduced to the code the intervals of the parameters reported in Table 6 as uniform distributions, thus, giving the same weight to all the values in each interval. The exception

Table 6
Clumpy Model Parameters and Considered Intervals

Parameter	Abbreviation	Interval
Radial extent of the torus	Y	15
Width of the angular distribution of clouds	σ	$[15°, 75°]$
Number of clouds along the radial equatorial direction	N_0	$[1, 15]$
Power-law index of the radial density profile	q	$[0, 3]$
Inclination angle of the torus	i	$[0°, 90°]$
Optical depth per single cloud	τ_V	$[10, 200]$

is the torus radial extent parameter Y, fixed as a Gaussian distribution centered at 15, with a width of 2.5. We fixed this parameter after confirming that it is otherwise unconstrained in the fits and is not correlated with any of the other parameters.[9] The choice of $Y = 15$ is justified below (Section 4.3.1). For those galaxies for which we have additional a priori knowledge about any of the parameters (e.g., the inclination angle of the torus for galaxies with known masers), the priors have been set as narrow Gaussians centered at a given value. Apart from the six parameters that characterize a clumpy model, there is another additional parameter that accounts for the vertical scale displacement, which we allow to vary freely, needed to match the fluxes of a chosen model to an observed SED. This vertical shift scales with the AGN bolometric luminosity (Section 5).

In order to compare with the observations, BAYESCLUMPY simulates the effect of the employed filters on the simulated SED by selecting the filter and introducing the observed flux and its corresponding error (assuming Gaussian errors). For a detailed description of the Bayesian inference applied to the clumpy models, see Asensio Ramos & Ramos Almeida (2009).

4.3. Model Results

4.3.1. Seyfert 2 Individual Fits

The results of the fitting process are the marginal posterior distributions for the six free parameters that describe the clumpy models and the vertical shift. These are the probability distribution of each parameter, represented as histograms. Uniform priors have been employed in our analysis of the observational data. Therefore, when the observed data introduce enough information into the fit, the resulting probability distributions will clearly differ from uniform distributions, either showing trends or being centered at certain values within the considered intervals.

We fit the individual Sy2 SEDs with the BAYESCLUMPY code, modeling only the torus emission, assuming no direct AGN continuum is detected. We also assume that foreground extinction from the host galaxy does not significantly modify the IR SEDs of the Seyfert galaxies in the sample. For example, Martini & Pogge (1999) used V–H colors of Sy2 galaxies in the CfA sample to derive levels of optical extinction up to $A_V \sim 5$ mag. Based on this, Alonso-Herrero et al. (2003) applied different values of A_V up to 5 mag to a subset of torus models (those of Efstathiou & Rowan-Robinson 1995) to illustrate the effects of dust in the host galaxy, and concluded that moderate amounts of foreground extinction ($A_V \lesssim 5$ mag) will not have a significant effect on the nuclear fluxes at $\lambda \gtrsim 2\,\mu$m. Thus, we do not consider foreground extinction in the fits with the clumpy models for the Seyfert galaxies in our sample. The only exception is Centaurus A, since its core is heavily

---

[9] The only exception is Centaurus A (which Y parameter results centered in ~10–15 without having constrained it. See the Appendix).

obscured by a dust lane up to $A_V \sim 7$–8 mag (Hough et al. 1987; Packham et al. 1996; Marconi et al. 2000). For details on the specific fit of this galaxy, see the Appendix.

The histograms corresponding to the probability distributions of the free parameters are shown in Figure 5 for Circinus, which constitutes the best fit in our sample. It also includes the histogram corresponding to the optical extinction produced by the torus along the LOS, computed as $A_V^{\mathrm{LOS}} = 1.086 N_0 \tau_V e^{(-(i-90)^2/\sigma^2)}$ mag.

We adopt a radial extent of $Y = 15$ as a Gaussian prior with a width of 2.5 because this parameter is otherwise unconstrained and presents no correlation with other parameters. The chosen value of $Y=15$ is consistent with all current observations of nearby active nuclei, which place the radial extent of the torus within values smaller than ~ 20–30 (Jaffe et al. 2004; Packham et al. 2005; Tristram et al. 2007; Meisenheimer et al. 2007; Radomski et al. 2008; Raban et al. 2009), and perhaps even as small as ~ 5–10. The lack of restriction of the torus radial extent is in agreement with the findings of Nenkova et al. (2008b), who report that IR SED fitting sets only a poor constraint on the torus size (see Section 5.3).

From Figure 5, it is clear that the Circinus data (eight photometric data points) provide sufficient information to constrain the model parameters. In addition to the above-mentioned prior for the Y parameter, we introduce a Gaussian prior on the inclination angle of the torus i, a Gaussian centered in $85°$, with a width of $2°$. We make this restriction in the i parameter because of the detection of a water vapor megamaser (Greenhill et al. 2003), which constrains the viewing angle to $i \sim 90°$. The optical depth per cloud results in a narrow Gaussian centered at the median value $\tau_V = 30 \pm 2$. The number of clouds results in a Gaussian-like distribution of median value $N_0 = 10 \pm 2$, and the width of the angular distribution has a median value of $\sigma = 61° \pm 8°$. Finally, we establish a lower limit of $q > 2.4$ at a 68% confidence level. The optical obscuration produced by the torus along the LOS would be of $A_V^{\mathrm{LOS}} = 320 \pm^{80}_{55}$ mag.

Although the solution to the Bayesian inference problem are the probability distributions shown in Figure 5, we translate these results into corresponding spectra (Figure 6). The maximum a posteriori (MAP) values of the parameters (i.e., the modes) represent the "best fit" to the data, since the mode corresponds to the most probable value of each parameter, and we plot the corresponding spectrum as a solid line. The dashed line shows the spectral model obtained using the median value of the probability distribution of each parameter, which is characteristic of the observed SED. Finally, the shaded region indicates the range of models compatible with a 68% confidence interval for each parameter around the median value. The observed Circinus SED is extremely well fitted with the clumpy models, including only the reprocessed torus emission without any stellar contribution. The model fitting to the photometric points makes a spectroscopic prediction: the 10 μm silicate feature appears in shallow absorption in the fitted models, as expected for Sy2 galaxies (Hao et al. 2007; Levenson et al. 2007). In particular, the model prediction for Circinus is in qualitative agreement with spectroscopic observations (Roche et al. 2006; Tristram et al. 2007) that show the silicate feature in absorption, although deeper than the predicted by the models (see the Appendix).

The excellent fit of the Circinus SED is the result of the combination of the good behavior of the clumpy models and the accuracy of the IR nuclear fluxes. The near-diffraction-limited adaptive optics NACO/VLT near-IR data (providing resolution between $0.''1$ and $0.''2$) and the T-ReCS/Gemini-South
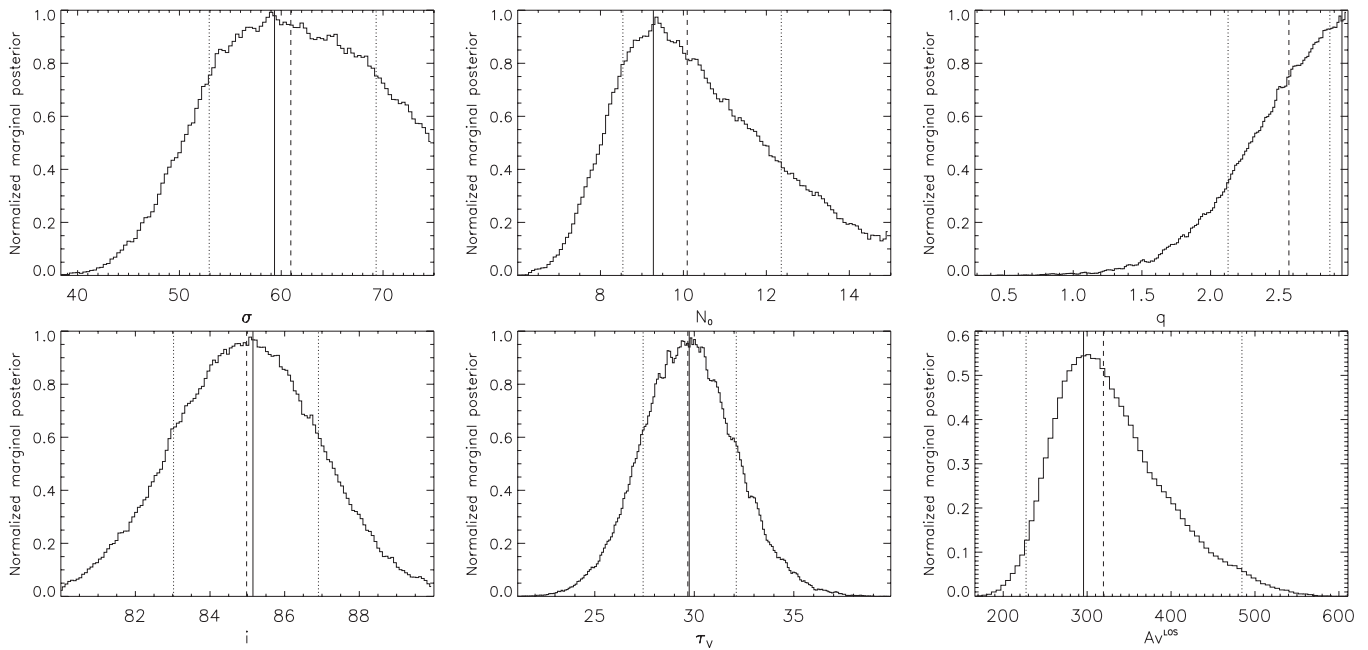
Figure 5. Probability distributions of the free parameters that describe the clumpy models resulting from the fit of Circinus, together with the calculated value of the optical extinction along the LOS A_V^{LOS}. The vertical shift and the Y parameter have been marginalized. Solid lines represent the mode of each distribution, dashed lines correspond to the median, and dotted lines indicate the 68% confidence level for each parameter around the median.
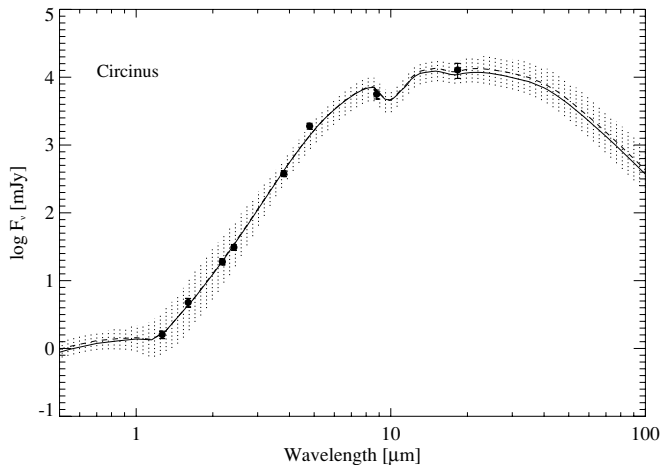

Figure 6. High spatial resolution Circinus SED. The solid line represents the "best fit" to the data, corresponding to the clumpy model described by the combination of parameters that maximizes the probability distributions of the parameters. The dashed line represents the model that corresponds to the median value of the probability distribution of each parameter. The shaded region indicates the range of models compatible with a 68% confidence interval for each parameter around the median.

mid-IR data (resolution between $0\rlap{.}''3$ and $0\rlap{.}''5$), together with the proximity of the galaxy provide the least contaminated (by host galaxy emission) SED of our sample, and consequently the best example of an AGN-dominated SED.

We apply the same technique to all the Sy2 individual galaxy measurements (with the exception of NGC 5728, for which we did not find near-IR nuclear fluxes in the literature, resulting then excluded from any further analysis), and plot the spectral results in Figure 7. The probability distributions of each parameter for all the individual galaxies are summarized in Table 7. Comments on the individual fits of the Sy2 galaxies in our sample are reported in the Appendix. Despite the more limited flux measurements in most individual cases, the resulting model

fits are generally good. The fitted parameters are consistent with unified AGN schemes and the requirement that the central engine be hidden from direct view in Type-2 AGNs. The only exceptional cases are NGC 1808 and NGC 7582, as both exhibit intense nuclear star formation and have lower spatial resolution mid-IR measurements (obtained at the CTIO 4 m). Thus, we consider these two model results unreliable, especially that of NGC 7582.

From the individual fits with the clumpy models, we infer the following conclusions. (1) For the majority of the Sy2 considered here, the clumpy models reproduce the observed SEDs, suggesting that the high spatial resolution measurements are dominated by the reprocessed emission of the torus. (2) The 10 μm silicate feature appears in absorption in the fitted models for seven out of the eleven Sy2 (Figure 7) and is practically flat in the case of NGC 7172. The unreliable NGC 1808 and NGC 7582 results, and also the Centaurus A fit suggest silicate emission. This is probably related with a characteristic SED shape, characterized by a low N/Q ratio plus L band excess (associated with stellar contamination). See Section 5.2 for details. (3) The average number of clouds along an equatorial ray is typically within the interval $N_0 = [5, 15]$. The exceptions are Centaurus A ($N_0 = 2 \pm 1$) and NGC 7582 ($N_0 < 2$). (4) High values of σ are preferred from our fits ($\sigma = [50, 75]$). We only find values of $\sigma < 40$ for the galaxies Mrk 573, NGC 1808, and NGC 7582. (5) High values of the inclination angle of the torus are preferred, with $i > 40°$, in general. (6) The combination of i, σ, and N_0 determines the likelihood of encountering a cloud along the line of sight to the central engine. In these cases, such encounters are always likely, which is consistent with having the AGN blocked from direct view, as expected in these Sy2. (7) Relatively low values of τ_V ($\leqslant 100$) are found. The exception here are Centaurus A and NGC 1808, for which we find $\tau_V > 100$. (8) The radial density profile q does not show any clear trend, and we find both low- and high-values within the considered interval. All the above-mentioned intervals or limits of the parameters correspond to median values. The reason for
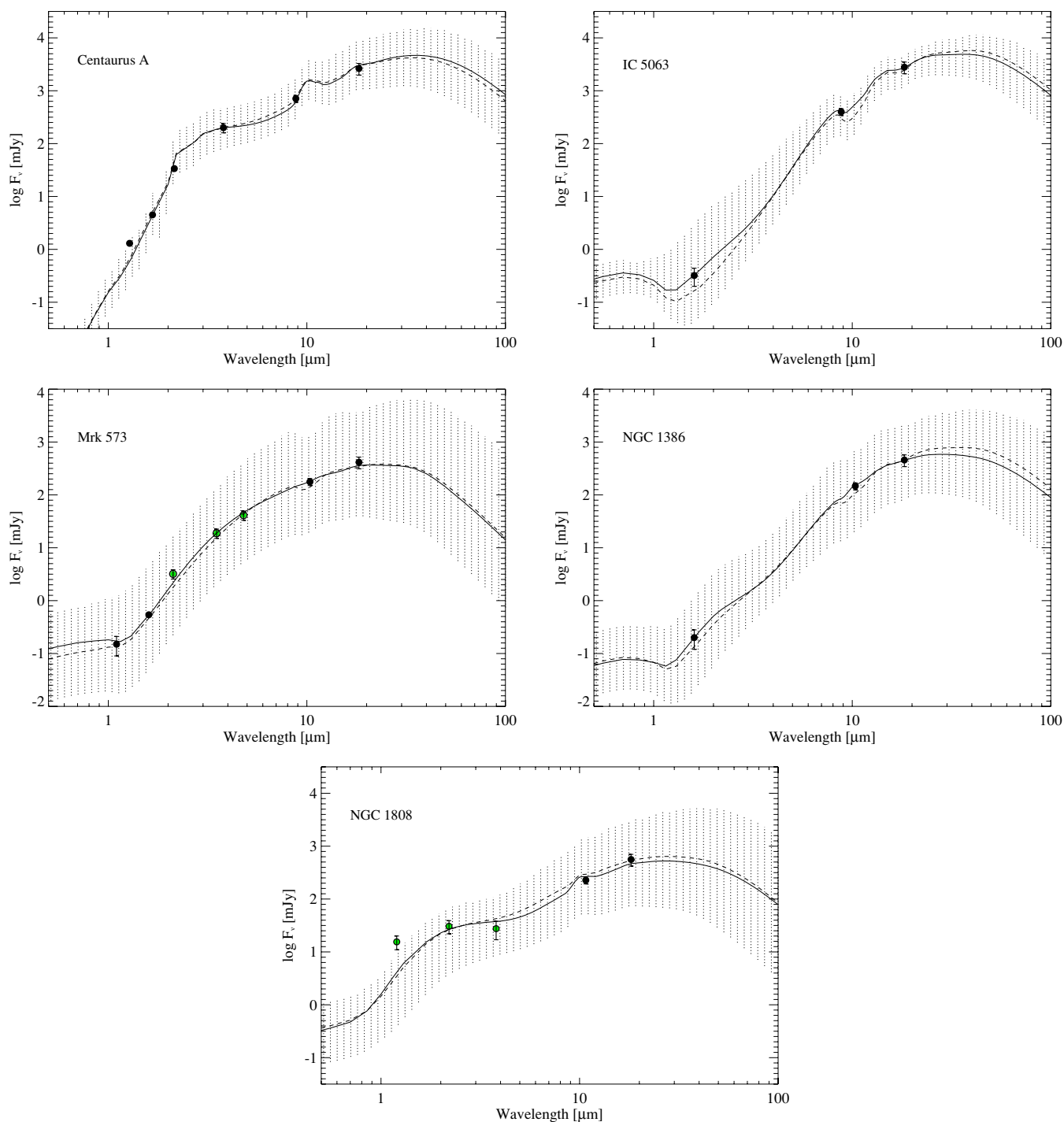
Figure 7. High spatial resolution SEDs of the Sy2 galaxies. Solid lines correspond to the model described by the combination of parameters that maximizes their probability distributions. Dashed lines represent the model computed with the median value of the probability distribution of each parameter. Shaded regions indicate the range of models compatible with the 68% confidence interval for each parameter around the median. Green dots correspond to seeing-limited near-IR data.

(A color version of this figure is available in the online journal.)

choosing median values instead of modes is that the median gives a less biased information about the result, since it takes into account degeneracies, while the mode does not.

4.3.2. Intermediate-type Seyfert Individual Fits

We fit the Sy1.8 and Sy1.9 nuclei the same way we fit the Sy2 SEDs, namely considering only the reprocessed torus emission. The optically broad lines and the relatively strong near-IR fluxes of the Sy1.5, however, suggest that some direct AGN

contribution is also present in these cases. Thus, we include the intrinsic AGN emission as a broken power law in these models. The AGN scales self-consistently with the torus flux, and additional extinction (separate from the clumpy torus) is a free parameter. The resulting fits are plotted in Figure 8. The Sy1 NGC 1566 is not included in the following because of the lack of near-IR nuclear fluxes in the literature for it.

From the individual fits of the intermediate-type Seyfert galaxies with the clumpy models, we find similarities and
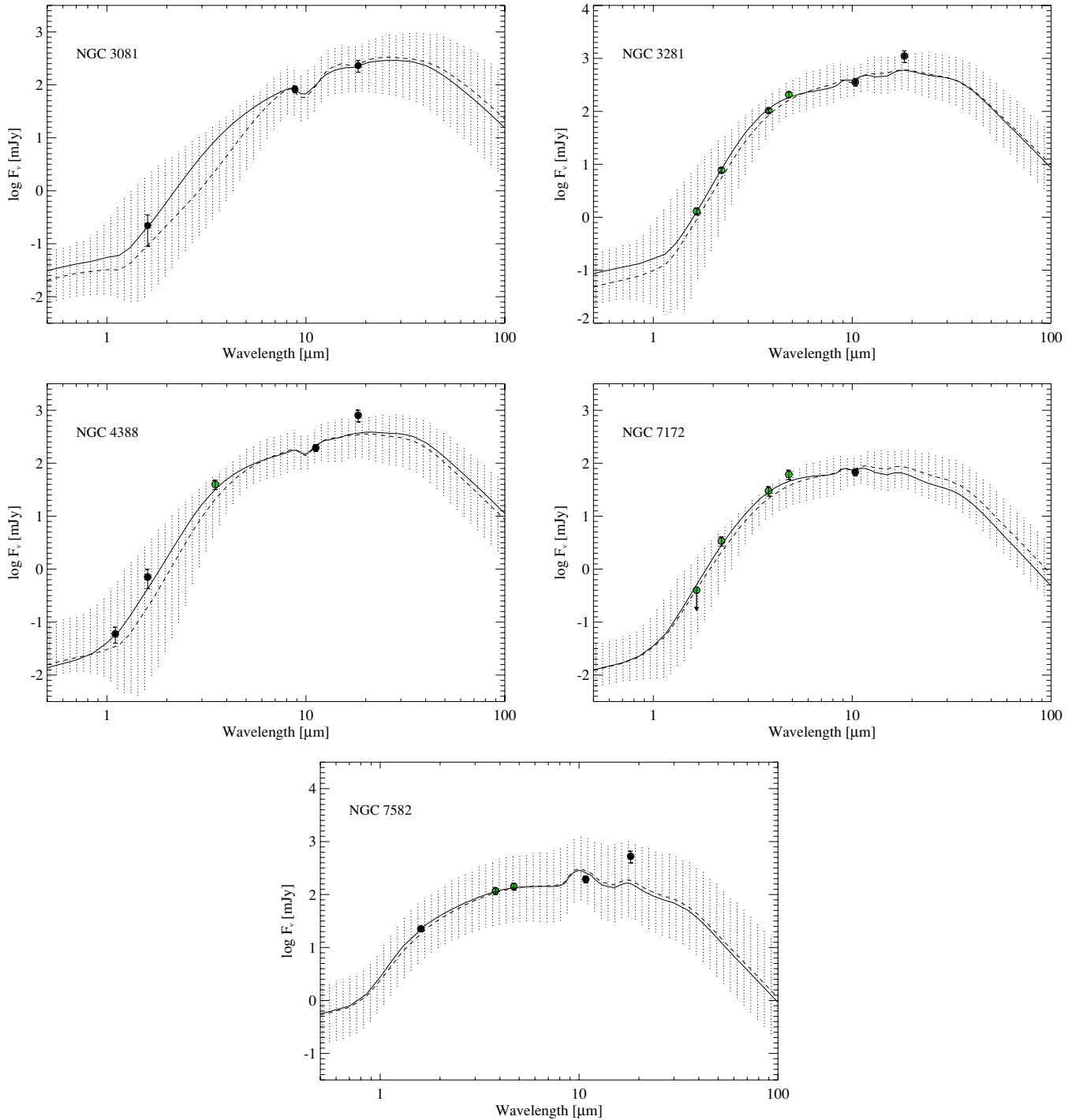
Figure 7. (Continued.)

(A color version of this figure is available in the online journal.)

differences with the Sy2 results. (1) Compared with the Sy2, lower values of σ are preferred in the fits of both the Sy1.8 and Sy1.9 ($\sigma = [25, 45]$) and Sy1.5 ($\sigma < 35$). (2) All the intermediate-type Seyferts result in a low number of clouds along the equatorial plane ($N_0 = [1,7]$). (3) Low values of the inclination angle of the torus are found for Sy1.5 ($i < 50°$) and also for the Sy1.8 NGC 1365. (4) q does not show any clear trend for intermediate-type Seyferts, and both low- and high-values within the considered interval are found, as for Sy2. (5) Low values of the optical depth per cloud are found for the two Sy1.9 galaxies ($\tau_V < 70$), while for the Sy1.8 and Sy1.5, high values ($\tau_V > 100$) are preferred. (6) In contrast with the wide range of values of the optical extinction produced by the torus for Sy2, all the intermediate-type Seyferts show $A_V \lesssim 200$ mag. (7) Including some obscured AGN contribution fits the near-IR excess of the observed SEDs of the Sy1.5 NGC 4151 and NGC 3227. The AGN is obscured by up to a few magnitudes at V in each case. (8) Except for the case of NGC 2992, for which both the data and the fit are very similar to those of Sy2 galaxies, the 10 μm silicate feature appears either in weak emission or

Table 7
Parameters Derived from the Clumpy Model Fitting

Galaxy	Seyfert Type	σ Median	σ Mode	N_0 Median	N_0 Mode	q Median	q Mode	i Median	i Mode	τ_V Median	τ_V Mode	A_V^{LOS} Median	A_V^{LOS} Mode
Centaurus A	2	$58\pm^{10}_{15}$	62	2 ± 1	1	<0.2	0.1	>85	89	$176\pm^{16}_{25}$	186	$300\pm^{100}_{80}$	260
Circinus	2	61 ± 8	59	10 ± 2	9	>2.4	3.0	85 (fix)	85	30 ± 2	30	$320\pm^{80}_{55}$	295
IC 5063	2	>57	75	>11	14	<1.5	0.4	>65	89	$70\pm^{31}_{23}$	66	$780\pm^{485}_{345}$	580
Mrk 573	2	<37	19	$6\pm^{5}_{2}$	4	<1.4	0.1	85 (fix)	85	$30\pm^{10}_{8}$	27	$185\pm^{120}_{75}$	150
NGC 1386	2	$50\pm^{16}_{19}$	51	11 ± 3	12	$1.5\pm^{0.9}_{1.0}$	2.1	85 (fix)	85	$95\pm^{66}_{51}$	51	<1460	410
NGC 1808	2	<35	16	$8\pm^{5}_{4}$	5	1.2 ± 0.9	0.9	$37\pm^{19}_{23}$	44	$146\pm^{37}_{50}$	198	<140	10
NGC 3081	2	>52	74	10 ± 3	11	>1.2	2.9	>42	89	$47\pm^{42}_{23}$	34	<450	120
NGC 3281	2	>68	75	$6\pm^{4}_{2}$	5	$1.3\pm^{1.1}_{0.8}$	0.6	>49	88	<12	10	$55\pm^{18}_{15}$	50
NGC 4388	2	>53	74	$9\pm^{4}_{3}$	7	<1.6	0.2	>38	88	<14	10	<80	50
NGC 7172	2	>54	74	$5\pm^{3}_{1}$	5	>1.7	2.9	>45	89	<12	10	50 ± 20	50
NGC 7582	2	<29	16	<2	1	>2.5	3.0	$41\pm^{19}_{28}$	58	<27	14	<6	1
NGC 1365	1.8	$35\pm^{20}_{13}$	31	$7\pm^{5}_{4}$	3	<1.7	0.1	<42	7	110 ± 60	88	<170	10
NGC 2992	1.9	$45\pm^{18}_{21}$	52	$7\pm^{5}_{3}$	4	<1.0	0.1	>53	85	$36\pm^{14}_{11}$	31	$160\pm^{130}_{80}$	130
NGC 5506	1.9	$25\pm^{9}_{7}$	15	<2	1	$2.5\pm^{0.3}_{0.4}$	2.7	85 (fix)	85	<68	22	<90	30
NGC 3227	1.5	$33\pm^{20}_{12}$	23	$6\pm^{5}_{4}$	3	<2	0.1	<48	14	115 ± 55	77	<210	10
NGC 4151	1.5	<32	16	<3	1	$1.7\pm^{0.8}_{0.9}$	1.9	$41\pm^{23}_{28}$	52	$120\pm^{55}_{48}$	93	<65	10

Notes. The Y parameter is fixed to be a Gaussian distribution centered at 15 with a width of 2.5. For the galaxies Circinus, Mrk 573, NGC 1386, and NGC 5506 the i parameter is also introduced as a Gaussian prior into the computations, centered at 85° with a width of 2°, based on other observations. Probability distributions presenting a single tail have been characterized with the mode and upper/lower limits at 68% confidence. Sy1.8 and Sy1.9 have been fitted with the geometry corresponding to torus emission-only. The Sy1.5 models include the intrinsic AGN continuum emission. The Sy2 NGC 5728 and the Sy1 NGC 1566 are not included here because of the lack of near-IR nuclear fluxes for them, preventing the SED fitting.

is absent in the intermediate-type Seyfert fits. As in Section 4.3.1, the values of the parameters above mentioned correspond to the median. Although the results from the modeling of Sy2 and intermediate-type Seyfert SEDs seem to point to different trends in their torus parameters, a larger set of objects is needed to clarify if these differences are really significant.

The results of our SED modeling of Seyfert galaxies are generally in good agreement with the findings of Nenkova et al. (2008b), who reproduce IR observations of both Type-1 and Type-2 Seyferts from the literature (Sanders et al. 1989; Elvis et al. 1994; Alonso-Herrero et al. 2003; Prieto et al. 2004; Mason et al. 2006; Hao et al. 2007; Netzer et al. 2007) using clumpy torus models. They find $N_0 \sim$ 5–15 clouds, $\tau_V \sim$ 30–100, $\sigma \sim$ 30°–50°, and the angular distribution of the clouds having a soft edge (the only distribution we consider here), with $q = 1$ or 2. They reproduce the observational data with compact torus sizes ($Y \sim$ 5–10), although they claim that the radial extent of the torus is poorly constrained from SED fitting.

5. INTERPRETATION OF OBSERVATIONS AND MODEL FITS

5.1. NIR Flux and Torus Inclination

The intermediate-type Seyferts exhibit characteristically higher H/N ratios, and the Sy1.5 have flatter SEDs overall. Hot dust emission from the directly illuminated faces of the clumps close to the central engine contributes to the near-IR emission in all these cases. In addition, the Sy1.5 include a component of the direct AGN emission (i.e., the tail of the optical/ultraviolet power-law continuum), which strongly flattens their IR SEDs.

In general, the relative near-IR flux depends sensitively on the torus inclination angle. The individual Sy2 show the same trend toward low near- to mid-IR ratios and therefore more edge-on views ($i > 40°$ considering the median values of the i distributions, and $i \sim 90°$ considering the modes). Only the unreliable measurements for NGC 7582 and NGC 1808 show

high near- to mid-IR ratios and thus indicate more pole-on views. In the context of the clumpy models, the presence of a cloud along the line of sight, which may occur from any viewing angle, results in Sy2 classification. Cloud encounters are more likely at large inclination angle, and thus we generally find larger values of the inclination angle for the Sy2. However, we do not suggest that all Sy2 are viewed exactly through the equatorial plane. This small sample includes a number of galaxies whose tori are known to be nearly edge-on (Circinus, Mrk 573, NGC 1386, and NGC 5506). Hence there is a selection bias for highly inclined tori in our sample.

The likelihood of a cloud encounter more completely depends on the combination of viewing angle, N_0, and σ. The preference for somewhat lower values of i, N_0, and σ in the intermediate-type Seyferts suggests that they present fewer clouds along the line of sight, even allowing some direct detection of the AGN continuum in the case of the Sy1.5. This configuration also increases the likelihood of unimpeded views of some directly illuminated cloud faces (i.e., those on the "back" side of the torus), which increases the near-IR flux. These selection effects may account for our finding of larger values of σ in the Sy2 sample than Nenkova et al. (2008b) report as typical for all Seyfert types ($\sim30°$), based on population statistics of Seyfert 1 and 2 galaxies (Schmitt et al. 2001; Hao et al. 2005a).

5.2. Stellar Contamination in the Near-IR?

One characteristic spectral shape the models cannot reproduce well exhibits both strong emission toward the long-wavelength end of the near-IR (around L band) and simultaneously a steep N/Q ratio. NGC 4388 is the most severe example of this problem; NGC 3281, NGC 5506, and NGC 7172 show similar effects. Because the formal uncertainties on the near-IR points are smaller than those at Q, the model fits tend to reproduce the near-IR measurements, while underpredicting the emission at Q in these cases. (While we do not observe NGC 7172 at Q directly, the models would not accommodate the
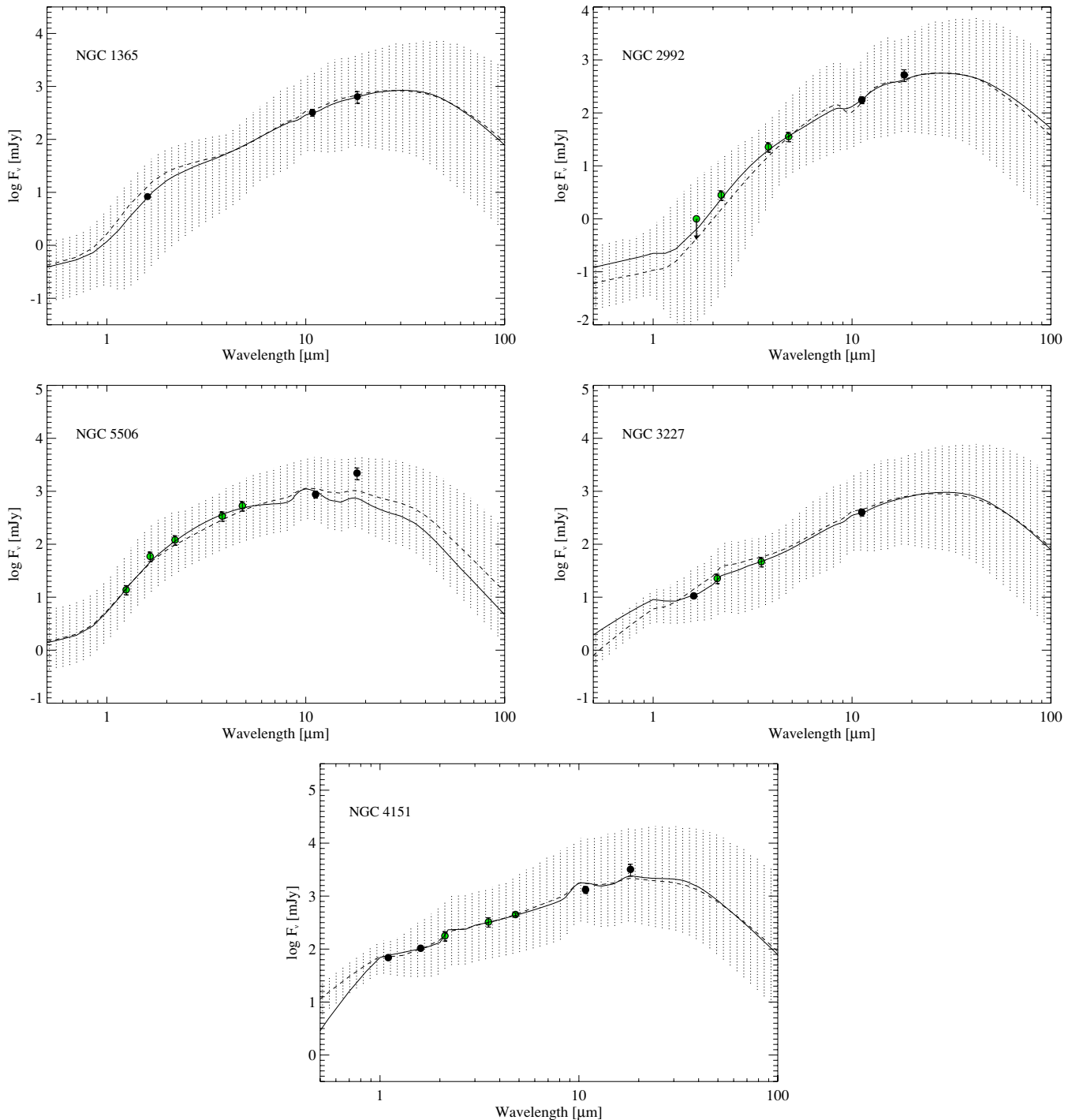
Figure 8. Same as in Figure 7 but for the intermediate-type Seyferts.
(A color version of this figure is available in the online journal.)

strong L band emission combined with a rise of the SED toward 20 μm, assuming a typical N/Q ratio.)

We can interpret these results either as a failure of the models or as evidence for near-IR contamination. In the former, the models require some modification to produce additional L band emission without otherwise altering the spectral shapes significantly. However, the fact that the most severe discrepancies arise in the galaxies that have the lowest resolution near-IR measurements suggests instead that stellar or other extended contributions can be significant even longwards of 2 μm. The L band observations of NGC 3281, NGC 4388, NGC 5506, and

NGC 7172 were obtained with natural seeing on 3 and 4 m telescopes, so even these "nuclear" fluxes cover scales up to 150 pc.

The possibility of stellar or other contamination of the Q band fluxes cannot be discarded, especially those from the 4 m CTIO. Where strong stellar emission takes place in the nuclear region of the galaxies, the emission of hot dust heated by this intense star formation is an important contribution at $\sim$20 μm (see, e.g., Helou et al. 2004; Mason et al. 2007). Alternatively, the NLR can contribute more strongly at longer wavelengths, as the models of Groves et al. (2006) show.

For the CTIO observations the resolution achieved in the Q band was ∼1″, which corresponds to physical scales up to ∼100 pc (in NGC 1365, NGC 1808, and NGC 7582). On the other hand, for the Gemini data the resolutions are between 0″.5 and 0″.6 in the Q band. Depending on the distance of each source, this implies having resolution from ∼10 pc (e.g., Centaurus A and Circinus) to ∼150 pc (e.g., IC 5063, NGC 3281, and Mrk 573). Thus, the steep N/Q ratios that the models cannot correctly reproduce could be due to the combined effect of stellar contamination around both the L and Q bands, or NLR contamination that is preferentially more severe at Q.

5.3. Torus Size

While the IR SEDs do not constrain the size of the torus, they are consistent with the small torus of clumpy models, confined to scales less than 10 pc. Uniform density models require the dusty torus to extend over large dimensions, to provide cool dust that produces the IR emission (e.g., Granato & Danese 1994). Fundamentally, in smooth distributions, the dust temperature is a monotonic function of distance to the nucleus. In contrast, in a clumpy distribution, different dust temperatures can coexist at the same distance, including cool dust at small radii (Nenkova et al. 2002), so large tori are not necessary. Indeed, the flat probability distribution we found when allowing Y to be a free parameter (and as small as 5) explicitly shows that small tori can produce the IR emission we observe.

In the clumpy models, with a steep radial density distribution ($q = 2$), the SED is never sensitive to the outer torus extent because the majority of the clouds are located very close to the nucleus for all values of Y. With flatter radial profiles, more clouds are located farther from the central engine. These model SEDs are then sensitive to Y, but the variations are evident only at wavelengths longer than 20 μm. Far-IR spectral observations would provide useful constraints (Levenson et al. 2007), but high spatial resolution measurements will remain critical because the far-IR emission from dust that stars heat increases.

5.4. 10 μm Silicate Feature and Column Density Estimates

The model fits to the photometric data yield spectral predictions. The 10 μm silicate feature is of particular interest. It is always weak (in emission or absorption) in the clumpy models, unlike smooth-density distributions in which it can appear in deep absorption (Dullemond & van Bemmel 2005; Levenson et al. 2007; Nenkova et al. 2008b). Fundamentally, the weak silicate feature arises in the clumpy model because both illuminated and dark cloud sides contribute to the observed spectrum. While most views of the Sy2 torus are through absorbing dark cloud faces, silicate emission from some bright faces fills in the feature, making it shallower. The weak silicate absorption or emission observed in Seyfert spectra indicate that a clumpy medium is the dominant source of obscuration (Levenson et al. 2007). Indeed, at high spatial resolution, where AGN emission is practically isolated, the silicate absorption has never been observed to be deep in Seyfert galaxies (Roche et al. 2006). The clumpy models reproduce the general observed trends of silicate emission in quasars and absorption in obscured Seyfert galaxies (Roche et al. 1991; Weedman et al. 2005; Hao et al. 2005b; Siebenmorgen et al. 2005; Sturm et al. 2005; Levenson et al. 2007). They can also accommodate the exceptional observations of silicate absorption in unobscured AGNs (Roche et al. 1991) and emission in buried AGNs (Mason et al. 2009), with different clump distributions.

We quantify the model silicate feature with its strength, which we define as $\tau_{10\,\mu m}^{app} = \ln(F_{cont}) - \ln(F_{core})$, relative to the underlying continuum. We calculate F_{cont} using a spline fit and F_{core} allowing peak wavelength to vary, following Sirocky et al. (2008). The values of $\tau_{10\,\mu m}^{app}$ are reported in Table 8. The silicate feature appears in shallow absorption in the fitted spectra of seven out of the eleven Sy2. The remaining four sources are Centaurus A, NGC 7172, and the unreliable cases of NGC 1808 and NGC 7582. All of them, except NGC 1808, have published mid-IR spectra that show the silicate feature in absorption, contrary to our results (see the Appendix for references). Excluding NGC 1808 and NGC 7582, the incorrect prediction of the silicate feature in very weak emission (practically flat) for NGC 7172 is probably due to the stellar contamination of the seeing-limited near-IR data described in Section 5.2. Indeed, the lack of Q band data for this galaxy limits the effectiveness of the modeling. The case of Centaurus A is more complicated, since the nuclear fluxes come from a ≲10 pc region, but the clumpy models reproduce the silicate feature in emission. This could be related to the controversial nature of the near- and mid-IR emission of this galaxy. According to several publications, synchrotron emission is significant or even dominant (Bailey et al. 1986; Turner et al. 1992; Chiaberge et al. 2001; Meisenheimer et al. 2007), although Radomski et al. (2008) argue instead that the synchrotron contribution to the mid-IR flux is small. For a detailed discussion of Centaurus A infrared emission nature and comparison with mid-IR spectroscopic data, see the Appendix.

Regarding the intermediate-type Seyferts, the silicate feature appears in weak emission or absent, except for the case of NGC 2992 (a Sy1.9 with a SED very similar to those of Sy2; see Table 5), for which it is in absorption. In general, all the predicted silicate features, either in emission or absorption, are weak, which is a consequence of the contribution of both illuminated and shadowed cloud faces that the clumpy models predict for all the geometries considered.

For the OHMc dust extinction profile (Ossenkopf et al. 1992), we can derive the apparent optical extinction using $A_V^{app} = \tau_{10\,\mu m}^{app} \times 23.6$ for the galaxies with the silicate feature in absorption (Table 8; Column 2). This value can be compared with the optical extinction along the LOS derived from our fits using the mode values of N_0, σ, τ_V, and i parameters (A_V^{LOS}, Table 7). Modes are used here instead of medians in order to avoid lower limits that would make more complicated the comparison with A_V^{app}. As expected, we obtain $A_V^{LOS} \gg A_V^{app}$ (see Table 8) since on the basis of the clumpy models, the true optical depth along LOS does not coincide with the apparent optical depth measured from the absorption silicate feature (A_V^{app}). The directly illuminated faces of the clouds seen along the LOS refill the absorption silicate band (produced by the obscuring material), thus producing lower apparent optical depth values. On the other hand, A_V^{LOS} takes into account the full model cloud distribution along the LOS.

The columns of material implied in the X-ray absorption (Table 8; Column 5) should be in principle comparable to or larger than those inferred from the fit of IR data with the models (Table 8; Column 4). Thus, we estimated N_H^{LOS} from the optical depth along the LOS, using the relationship $N_H^{LOS}/A_V^{LOS} = 1.9 \times 10^{21}$ cm^{-2} mag^{-1} from Bohlin et al. (1978). Larger absorbing column densities derived from X-ray measurements (N_H^{X-ray}) compared with N_H^{LOS} suggest that the X-ray-emitting regions are affected by a larger amount of extinction than the mid-IR ones. As it was first noted by Granato

Table 8
Silicate Feature Predictions

Galaxy	$\tau_{10\,\mu\mathrm{m}}^{\mathrm{app}}$	A_V^{app} (mag)	A_V^{LOS} (mag)	N_H^{LOS} (cm^{-2})	$N_H^{\mathrm{X-rays}}$ (cm^{-2})	Reference(s)
Centaurus A	−0.67	⋯	260	4.9×10^{23}	1.5×10^{23}	a
Circinus	0.86	20	295	5.6×10^{23}	4.0×10^{24}	b
IC5063	0.94	22	580	1.1×10^{24}	2.6×10^{23}	c
Mrk 573	0.44	10	150	2.8×10^{23}	$>1.0 \times 10^{24}$	d
NGC 1386	0.41	10	410	7.8×10^{23}	1.5×10^{24}	e
NGC 1808	−0.21	⋯	10	1.9×10^{22}	3.1×10^{22}	f
NGC 3081	0.91	21	120	2.3×10^{23}	6.3×10^{23}	d
NGC 3281	0.21	5	50	9.5×10^{22}	2.0×10^{24}	g
NGC 4388	0.51	12	50	9.5×10^{22}	2.6×10^{23}	h
NGC 7172	⋯	⋯	50	9.5×10^{22}	8.3×10^{22}	i
NGC 7582	−0.61	⋯	1	1.9×10^{21}	1.4×10^{23}	j
NGC 1365	0.00	⋯	10	1.9×10^{22}	4.8×10^{23}	k
NGC 2992	0.74	17	130	2.5×10^{23}	8.0×10^{21}	l
NGC 5506	−0.21	⋯	30	5.7×10^{22}	3.6×10^{22}	m
NGC 3227	−0.09	⋯	10	1.9×10^{22}	5.3×10^{22}	n
NGC 4151	−0.31	⋯	10	1.9×10^{22}	6.9×10^{22}	o

Notes. Silicate strength $\tau_{10\,\mu\mathrm{m}}^{\mathrm{app}}$ measured from the fitted models; negative values indicate a silicate feature in emission. It was not possible to properly measure $\tau_{10\,\mu\mathrm{m}}^{\mathrm{app}}$ for NGC 7172 because the feature is in extremely weak emission, and self-absorbed. Corresponding apparent optical extinction, A_V^{app}, assumes $A_V^{\mathrm{app}}/\tau_{10\,\mu\mathrm{m}}^{\mathrm{app}} = 23.6$, and A_V^{LOS} comes from the modeling. N_H^{LOS} is calculated from $N_H/A_V^{\mathrm{LOS}} = 1.9 \times 10^{21}\mathrm{cm}^{-2}\mathrm{mag}^{-1}$ (Bohlin et al. 1978). $N_H^{\mathrm{X-ray}}$ values are taken from the literature.
References. (a) Markowitz et al. 2007; (b) Soldi et al. 2005; (c) Turner et al. 1997; (d) this work; (e) Levenson et al. 2006; (f) Jiménez-Bailón et al. 2005; (g) Vignali & Comastri 2002; (h) Elvis et al. 2004; (i) Awaki et al. 2006; (j) Turner et al. 2000; (k) Risaliti et al. 2005; (l) Yaqoob et al. 2007; (m) Lamer et al. 2000; (n) Lamer et al. 2003; (o) Beckmann et al. 2005.

et al. (1997), dust-free absorption unrelated to the torus could be the main source of X-ray obscuration. Thus, the X-ray absorber would be gas located inside the dust sublimation radius. This is the case for most of the sample, with $N_H^{\mathrm{X-ray}}/N_H^{\mathrm{LOS}}$ ranging from 2 to 25 (excluding the unrealistic NGC 7582 result). In contrast, comparable values of N_H^{LOS} and $N_H^{\mathrm{X-ray}}$ (those of Centaurus A, NGC 7172, and NGC 5506) mean that the dust-free absorption in these galaxies is low. We derive unrealistic results for IC 5063 and NGC 2992, for which $N_H^{\mathrm{X-ray}} < N_H^{\mathrm{LOS}}$. This could be due to the known intrinsic X-ray variability of these galaxies (Polletta et al. 1996; Turner et al. 1997; Yaqoob et al. 2007; Gilli et al. 2000). In the case of variable sources, we cannot directly compare the column density predictions from IR data modeling and X-ray measurements, since the data have not been taken simultaneously.

5.5. AGN Luminosities

The clumpy model fits yield the bolometric luminosity of the intrinsic AGN in each case. Combining this value with the torus luminosity, we derive the reprocessing efficiency of the torus. The vertical shift parameter scales with AGN luminosity, which we report in Table 9 ($L_{\mathrm{bol}}^{\mathrm{AGN}}$; Column 1) for the median models. Integrating the corresponding model torus emission yields the torus luminosity ($L_{\mathrm{bol}}^{\mathrm{tor}}$; Column 2).

The Sy2 tori in our sample are efficient reprocessors, absorbing and re-emitting the majority of the intrinsic AGN luminosity in the IR (with mean efficiency 0.6 ± 0.3). Among the Sy2, only Centaurus A, Mrk 573, and the unreliable results of NGC 1808 and NGC 7582 indicate efficiencies below 50% (the mean efficiency is 0.7 ± 0.3, excluding NGC 1808 and NGC 7582). With the limited sample size, the efficiencies of the intermedi-

ate types (0.4 ± 0.3) are formally comparable to those of Sy2, but the measurements point out that possibly Type-2 tori reprocess radiation more efficiently than Type-1 tori, although the measured differences between both Seyfert types are not significant. A larger subset of Sy1 and intermediate-type Seyferts is needed to clarify if tori of different Seyfert types are genuinely different. The reprocessing fraction depends primarily on the total number of clouds available to absorb the incident radiation, which increases with the model parameters N_0 and σ. If all Seyfert nuclei are identical, only the viewing angle would change with the classification, not the properties of the torus itself. While these results are limited, they suggest instead that classification is biased. Specifically, when the torus covers a smaller fraction of the sky viewed from the central engine (which results in a lower efficiency), the galaxy is less likely to be classified as a Sy2 (because the AGN is incompletely blocked from more lines of sight). Such a selection effect would also extend to Sy1; IR observations of these galaxies would provide useful tests of this suggestion against strong forms of AGN unification.

The outer size of the torus scales with the AGN bolometric luminosity: $R_o = Y R_d$, so assuming a dust sublimation temperature of 1500 K, $R_o = 6(L_{\mathrm{bol}}^{\mathrm{AGN}}/10^{45})^{0.5}$ pc (with fixed $Y = 15$). We find that all tori in our sample have outer extents less than 5 pc (Table 9), in agreement with recent mid-IR direct imaging of nearby Seyferts (Packham et al. 2005; Radomski et al. 2008) and also interferometric observations (Jaffe et al. 2004; Tristram et al. 2007; Meisenheimer et al. 2007; Raban et al. 2009). Specifically, the estimated outer radii for Circinus ($R_o = 0.6$ pc) and Centaurus A ($R_o = 0.4$ pc) are close to the upper limits reported by Tristram et al. (2007) and Meisenheimer et al. (2007), of 1 and 0.3 pc, respectively. The uncertainty of these radial sizes is large, mostly because the unknown value of Y enters the

Table 9
Bolometric Luminosity Predictions

Galaxy	$L_{\mathrm{bol}}^{\mathrm{AGN}}$ (erg s^{-1})	$L_{\mathrm{bol}}^{\mathrm{tor}}$ (erg s^{-1})	$L_{\mathrm{bol}}^{\mathrm{tor}}/L_{\mathrm{bol}}^{\mathrm{AGN}}$	R_o (pc)	$L_{\mathrm{Xbol}}^{\mathrm{AGN}}$ (erg s^{-1})	$L_{\mathrm{Xbol}}^{\mathrm{AGN}}/L_{\mathrm{bol}}^{\mathrm{AGN}}$
Centaurus A	5.5×10^{42}	1.6×10^{42}	0.29	0.44	1.3×10^{43}	2
Circinus	1.0×10^{43}	8.1×10^{42}	0.81	0.60	1.2×10^{43}	1.2
IC 5063	2.4×10^{44}	2.1×10^{44}	0.87	2.94	1.7×10^{44}	0.7
Mrk 573	4.3×10^{44}	6.6×10^{43}	0.15	3.93	4.4×10^{44}	1.0
NGC 1386	3.4×10^{42}	2.0×10^{42}	0.59	0.35	1.3×10^{43}	4
NGC 1808	6.8×10^{42}	3.1×10^{42}	0.45	0.49	2.2×10^{41}	0.03
NGC 3081	1.0×10^{43}	8.9×10^{42}	0.89	0.60	1.0×10^{44}	10
NGC 3281	7.4×10^{43}	5.3×10^{43}	0.72	1.63	3.0×10^{44}	4
NGC 4388	2.1×10^{43}	1.7×10^{43}	0.81	0.87	1.5×10^{44}	7
NGC 7172	8.5×10^{42}	6.7×10^{42}	0.79	0.55	1.1×10^{44}	13
NGC 7582	1.1×10^{44}	1.1×10^{43}	0.10	1.99	9.8×10^{43}	0.9
NGC 1365	1.7×10^{43}	1.1×10^{43}	0.65	0.78	3.0×10^{43}	1.8
NGC 2992	2.8×10^{43}	1.5×10^{43}	0.53	1.00	3.0×10^{43}	1.1
NGC 5506	7.3×10^{44}	5.1×10^{43}	0.07	5.13	2.2×10^{44}	0.3
NGC 3227	2.0×10^{43}	1.1×10^{43}	0.55	0.85	3.8×10^{43}	1.9
NGC 4151	1.4×10^{44}	2.2×10^{43}	0.16	2.24	1.7×10^{44}	1.2

Notes. Bolometric luminosities corresponding to AGN luminosity and integrated flux of the model emission (i.e., reprocessed luminosity). Luminosities are good to a factor of 2. Columns 4 and 5 correspond to the fraction of energy emitted by the AGN that is reprocessed by the torus ($L_{\mathrm{bol}}^{\mathrm{tor}}/L_{\mathrm{bol}}^{\mathrm{AGN}}$) and outer radius of the torus calculated using $L_{\mathrm{bol}}^{\mathrm{AGN}}$. Absorption-corrected 2–10 keV X-ray luminosities are taken from the literature (references in Table 8). $L_{\mathrm{Xbol}}^{\mathrm{AGN}}$ is derived from $20 \times L_{\mathrm{X}}^{\mathrm{AGN}}$.

calculation linearly, but the consistency with other measurements further supports the assumption of $Y = 15$.

The bolometric luminosity of the intrinsic AGN derived from the fits (Table 9; Column 1) can be directly compared with the bolometric luminosities derived from the absorption-corrected 2–10 keV luminosities compiled from the literature (Table 9; Column 5). To get $L_{\mathrm{Xbol}}^{\mathrm{AGN}}$ from the intrinsic 2–10 keV luminosities, we applied a conversion factor of 20 (Elvis et al. 1994). In general, we find comparable values of $L_{\mathrm{Xbol}}^{\mathrm{AGN}}$ and $L_{\mathrm{bol}}^{\mathrm{AGN}}$ within the considered errors for $L_{\mathrm{bol}}^{\mathrm{AGN}}$. Exceptions are NGC 3081, NGC 4388, and NGC7172, for which $L_{\mathrm{Xbol}}^{\mathrm{AGN}} \sim 10 \times L_{\mathrm{bol}}^{\mathrm{AGN}}$, and the unreliable NGC 1808, in the opposite direction.

6. CONCLUSIONS

We report subarcsecond resolution mid-IR fluxes for 18 Seyfert galaxies. These nuclear fluxes, in combination with published near-IR measurements at comparable resolution are used to construct SEDs corresponding to torus emission. We analyze and fit these SEDs with the clumpy dusty torus models of Nenkova et al. (2002, 2008a, 2008b). The main results are summarized in the following.

1. The high spatial resolution mid-IR nuclear fluxes reported in this work provide a spectral shape of the individual SEDs that is different from that of large aperture data SEDs (on scales of a few arcseconds).

2. The shape of the average Sy2 SED, constructed using only pure Sy2 galaxies and either diffraction- or near-diffraction-limited data, rises steeply toward the mid-IR, with an IR slope (from ∼1 μm to 18 μm), $\alpha_{\mathrm{IR}} = 3.1 \pm 0.9$.

3. The individual Sy2 SEDs are typically steep through the IR, with α_{IR} ranging from 1.8 to 3.8. Considering separately the near-IR (from ∼1 to ∼9 μm) and the mid-IR (∼10 to ∼18 μm) slopes, we find $\alpha_{\mathrm{NIR}} \gtrsim \alpha_{\mathrm{MIR}}$, with $\alpha_{\mathrm{NIR}} = 3.6 \pm 0.8$ and $\alpha_{\mathrm{MIR}} = 2.0 \pm 0.2$ measured from the average Sy2 SED.

4. The IR SEDs of the intermediate-type Seyferts in the sample are flatter ($\alpha_{\mathrm{IR}} = 2.0 \pm 0.4$ for Sy1.8 and 1.9 and $\alpha_{\mathrm{IR}} = 1.6 \pm 0.3$ for Sy1.5) and present larger N/Q band ratios than those of Seyfert 2 galaxies. The near-IR excess that flattens the SED of all intermediate-type Seyferts is due to the contribution of hot dust from the illuminated faces of the clouds, while direct AGN emission is also important in the case of Sy1.5.

5. The clumpy models of Nenkova et al. (2008a, 2008b) successfully reproduce the SEDs of both the Seyfert 2 and the intermediate-type Seyferts. The models accommodate the range of α_{IR} observed in the former, while providing optically thick obscuration along the line of sight.

6. The IR SEDs do not constrain the radial extent of the torus, Y, and this parameter remains uncorrelated with the other parameters. Because the outer torus contains the coolest material, high angular resolution measurements at wavelengths longer than 15 μm are needed to reveal significant variations in the torus size.

7. In the individual Sy2 fits, we generally find the number of clouds within the interval $N_0 = [5, 15]$, the width of the angular distribution of clouds within $\sigma = [50°, 75°]$, high values of the inclination angle of the torus ($i = [40°, 90°]$), and optical depths per cloud $\tau_V < 100$. The radial density profile q does not show any clear trend within the considered interval ([0, 3]).

8. We find small number of clouds in the individual intermediate-type Seyfert fits ($N_0 = [1,7]$). Low values of σ are preferred from the fits of Sy1.8 and Sy1.9 ($\sigma = [25°, 50°]$) and even lower for Sy1.5 ($\sigma < 35°$). We require direct (though extinguished) emission of the AGN to reproduce the near-IR excess observed in the SEDs of Sy1.5.

9. Views of Sy2 are more inclined than those of the Sy1.5 galaxies. More importantly, the larger values of N_0 and σ in the Sy2 models suggest that these central engines are blocked from direct view along more lines of sight, in contrast to the intermediate-type Seyferts, which present

more clear views of the AGN. Due to the limited size of the analyzed sample, these differences are not significant.

10. Although the fits are based on photometric data, the models predict the behavior of the 10 μm silicate spectral feature. Most of the individual Sy2 galaxies show shallow silicate absorption. In all but one of the intermediate-type Seyferts, the feature is either in shallow emission or absent.

11. The columns of material responsible for the X-ray absorption are larger than those inferred from the model fits for most of the galaxies in the sample, which is consistent with X-ray absorbing gas located within the dust sublimation radius, whereas the mid-IR flux arises from an area farther from the accretion disk.

12. The combination of large number of clouds and high values of σ results in tori that more efficiently reprocess the incident nuclear radiation than those with lower values of these parameters.

13. In the models, the outer radial extent of the torus scales with the AGN luminosity, and we find the tori to be confined to scales less than 5 pc.

APPENDIX

INDIVIDUAL OBJECTS

Below, we comment on the individual fits of the galaxies in our sample, including Type-2 Seyferts and intermediate types. Unless the opposite is indicated, all the reported values from the fits correspond to or are calculated from the median values.

Centaurus A. Centaurus A (NGC 5128) is a nearby Sy2 nucleus, with its core heavily obscured by a dust lane. This makes it visible only at wavelengths longwards $\sim$1 μm (Schreier et al. 1998; Marconi et al. 2000). Indeed, Hough et al. (1987), Packham et al. (1996), and Marconi et al. (2000) determined a value for the extinction caused by the dust lane of $A_V \sim$ 7–8 mag. However, the total obscuration on our LOS to the core was estimated by Meisenheimer et al. (2007) to be $A_V \sim$ 14 mag, including the torus material. Due to the existence of the dust lane, that is probably affecting our nuclear fluxes (specially the near-IR ones), we exceptionally have taken this foreground extinction into account for the fit of Centaurus A with the clumpy models (Figure 7), by fixing $A_V = 8$ mag and applying the Calzetti et al. (2000) law to the fitted models.

The clumpy models reproduce the observed photometry very accurately, but not the broad absorption silicate feature detected in mid-IR spectroscopy and interferometry (Siebenmorgen et al. 2004a; Meisenheimer et al. 2007). This mismatch in the fitted model could be due to the synchrotron radiation contribution to the IR fluxes claimed by Bailey et al. (1986), Turner et al. (1992), Chiaberge et al. (2001), and Meisenheimer et al. (2007). Indeed, Meisenheimer et al. (2007) find from mid-IR interferometric observations that the contribution of synchrotron emission to the nuclear emission of Centaurus A is of $\sim$80% at $\sim$8 μm and $\sim$60% at $\sim$13 μm. However, the results of Radomski et al. (2008), including the lack of variability at $\sim$10 μm (see Radomski et al. 2008 and references therein) and zero polarization at $\sim$1 mm (although low millimeter polarization may be associated with low-luminosity sources; Packham et al. 1996) are inconsistent with a synchrotron source as that suggested by Meisenheimer et al. (2007). A more detailed analysis of the SED of this galaxy, e.g., including an optically thin power law in the fits to account for the synchrotron radiation can be done. However, this kind of detailed analysis of an individual galaxy is beyond the scope of this work.

The probability distributions derived from the fit of the Centaurus A SED with the clumpy models clearly constrain the number of clouds N_0, the optical depth of each cloud τ_V, and the width of the angular distribution σ. N_0 resembles a Gaussian distribution centered at the median value $N_0 = 2\pm1$. The τ_V histogram shows an asymmetric shape, with a tail toward low values and of median $\tau_V = 176$ at a 68% confidence level. High-σ values are more probable than others (median value of $58°\pm^{10}_{15}$), and the same for the inclination angle of the torus ($i > 85°$). In contrast, low values of q are preferred ($q < 0.2$). The radial thickness of the torus Y has been introduced to the code as a Gaussian prior centered in 15 with a width of 2.5, as explained in Section 4.2. Indeed, the preliminary fit of Centaurus

A without restrictions in any of the model parameters was the only one that constrained the radial thickness of the torus, with a median value of its probability distribution of $Y \sim 15$. The calculated median value of the optical extinction produced by the torus is $A_V^{LOS} = 300 \pm_{80}^{100}$ mag for this galaxy.

Circinus. The Circinus galaxy is a nearby Sy2 with a prominent cone-shaped region revealed in the [O III] images (Wilson et al. 2000). Both the accuracy of the eight high spatial resolution flux measurements and the proximity of the galaxy make the resulting fit excellent. Water vapor megamasers (Greenhill et al. 2003) constrain the viewing angle to $i \sim 90°$. Thus, in addition to the Gaussian prior for the Y parameter, we introduce a prior on i, a Gaussian centered in $85°$, with a width of $2°$.[10] The resulting fit constrains most model parameters. The optical depth per cloud results in a narrow Gaussian centered at the median value $\tau_V = 30 \pm 2$. The number of clouds results in a Gaussian-like distribution (median value of $N_0 = 10 \pm 2$), and the width of the angular distribution has a median value of $\sigma = 61° \pm 8°$. Finally, we establish a lower limit of $q < 2.3$ at a 68% confidence level. The optical obscuration produced by the torus would be $A_V^{LOS} = 320 \pm_{55}^{80}$ mag. Roche et al. (2006) found the core of Circinus compact and obscured by a substantial column of silicate dust from T-ReCS/Gemini-South spectroscopy. They obtained a value for the silicate absorption depth of $\tau_{10\,\mu m} = 1.6$. Our fitted models reproduce the silicate feature in absorption (see Table 8), in qualitative agreement with the observations, but shallower ($\tau_{10\,\mu m}^{app} = 0.86$) than that reported by Roche et al. (2006). We find that the absorption column density inferred from X-ray measurements ($N_H^{X-rays} = 4 \times 10^{24}$ cm^{-2}) is larger than that responsible for the mid-IR absorption ($N_H^{LOS} \sim 6 \times 10^{23}$ cm^{-2}). This is consistent with the X-ray obscuring region being closer to the central engine than the mid-IR emitting dust.

IC 5063. This Sy2 nucleus is hosted by a merger remnant classified as an elliptical galaxy (Colina et al. 1991). An obscuring dust lane partially covers the eastern side of the galaxy. A peculiarity of this source is its strong radio luminosity, which is 2 orders of magnitude larger than the typical values for Seyfert galaxies (Colina et al. 1991). From an N-band acquisition image of IC 5063 obtained with T-ReCS/Gemini-South, Young et al. (2007) tentatively found the nucleus of this galaxy slightly resolved. However, from our T-ReCS Si2 and Qa band imaging the nucleus appears unresolved, and consequently, we subtracted the corresponding PSF at the 100% level to derive the nuclear fluxes. From the fit with the clumpy models, we establish lower limits for three of the parameters ($\sigma > 57°$, $N_0 > 11$, and $i > 65°$) and an upper limit for the index of the radial density profile ($q < 1.5$). The only Gaussian-like distribution resulting from the fit corresponds to τ_V (median value of $70 \pm_{23}^{31}$). A_V^{LOS} is calculated to be $780 \pm_{345}^{485}$ mag. The galaxy presents one of the highest L_{bol}^{AGN} of the sample (2.4×10^{44} erg s^{-1}, see Table 9), and also a high reprocessing efficiency (87%), consistent with the large values of N_0 and σ we find. X-ray observations with the *ASCA* satellite allow us to infer an intrinsic 2–10 keV luminosity of $\sim 10^{43}$ erg s^{-1}, that is within the range expected for Seyfert 1 galaxies (Turner et al. 1997). The silicate feature appears in absorption in the fitted models, in qualitative agreement with mid-IR spectroscopic observations obtained with T-ReCS/Gemini-South (Young et al. 2007). However, the absorption band appears deeper in our

models ($\tau_{10\,\mu m}^{app} = 0.94$) than in the mid-IR spectrum ($\tau_{10\,\mu m} = 0.33$).

Mrk 573. Mrk 573 is optically classified as a classical Sy2 nucleus (Tsvetanov & Walsh 1992), and Ramos Almeida et al. (2008) recently re-classify it as an obscured NLSy1 galaxy, based on near-IR spectroscopy and X-ray archival data. The X-ray observations of Mrk 573 do not straightforwardly reveal the intrinsic luminosity of this AGN because it suffers from Compton thick obscuration (Guainazzi et al. 2005). The strong soft X-ray emission is likely photoionized line emission. It is not the AGN continuum in any case, so previous simplified fits of power-law models over a broad energy range (e.g., Guainazzi et al. 2005; Shu et al. 2007) fail to accurately measure the AGN. We determine the intrinsic AGN luminosity from the *XMM-Newton* observation of Mrk 573 with the pn detector, which offers a high S/N. We use the reduced data and associated background and calibration files from XAssist pipeline processing (Ptak & Griffiths 2003). We fit only the data at energies greater than 3 keV, to avoid confusion from the separate soft emission sources. The observed continuum is flat and the Fe Kα line equivalent width (EW) is large, which are characteristic of a purely reflected (not direct) AGN continuum. We fix the photon index $\Gamma = 0$ and find EW $= 2.0 \pm 0.7$ keV. The results are similar if a typical AGN continuum slope is adopted ($\Gamma = 1.9$). We follow the technique of Levenson et al. (2006), using the Fe line luminosity and EW and to determine the intrinsic AGN luminosity, finding $L_X^{AGN} = 2.2 \times 10^{43}$ erg s^{-1} in the 2–10 keV bandpass. We note that the fitted hard continuum directly corresponds to an intrinsic luminosity that is a factor of 100 smaller.

The IR SED shape of Mrk 573 is practically the same as those of the rest of Sy2 galaxies in the sample, so we consider it equivalent to the other Sy2. This galaxy presents a strong symmetric double radio lobe (Nagar et al. 1999), suggesting that it contains an edge-on torus; the radio lobes would be asymmetric if the jets were out of the plane of the sky. The SED fit reproduces all seven data points and also constrains the majority of the parameters. As for the case of Circinus, we have introduced the inclination angle of the torus as a Gaussian prior, centered in $85°$ with a width of $2°$. The probability distribution of N_0 present a Gaussian shape, with median value $N_0 = 6 \pm_2^5$ (there is a tail toward large values that enlarges the error). The σ and q distributions allow us to establish upper limits of $\sigma < 37°$ and $q < 1.4$. The optical depth of each cloud shows a Gaussian distribution with a median value of $\tau_V = 30 \pm_8^{10}$. The optical extinction produced by this clumpy torus is $A_V^{LOS} = 185 \pm_{75}^{120}$ mag. Mrk 573 has the highest L_{bol}^{AGN} of the Sy2 subset (4.3×10^{44} erg s^{-1}; Table 9), but due to the low values of N_0 and σ derived from its fit, its reprocessing efficiency is low ($\sim 15\%$). The 10 μm silicate feature appears in shallow absorption in the median-fitted model ($\tau_{10\,\mu m}^{app} = 0.44$; see Table 8), producing an estimated value of the optical extinction $A_V^{app} = 11$ mag. The hydrogen column density obtained from the modeling along the LOS ($N_H^{LOS} \sim 3 \times 10^{23}$ cm^{-2}) is much lower than the one that obscures the X-ray emission ($N_H^{X-rays} > 1 \times 10^{24}$ cm^{-2}).

NGC 1386. NGC 1386 is one of the nearest Sy2 galaxies and therefore extensively studied. Mauder et al. (1992) resolved its NLR on a $0\rlap.{''}3$ scale (~ 15 pc) using speckle interferometry, detecting individual NLR clouds and claiming a clumpy structure. The detection of a water vapor megamaser in NGC 1386 (Braatz et al. 1997) constrains the inclination angle of the torus to be $i \sim 90°$, as in the case of Circinus and Mrk 573. The fit

---
[10] We choose this value of i to allow for a narrow Gaussian distribution within the considered interval $[0°, 90°]$.

with the clumpy models reproduces the observed SED; we find $N_0 = 11 \pm 3$, $\sigma = 50°\pm^{16}_{19}$, $\tau_V = 95\pm^{66}_{51}$, and $q = 1.5\pm^{0.9}_{1.0}$ at a 68% confidence level. The optical extinction produced by the clumpy torus is $A_V^{\rm LOS} < 1460$ mag. The fitted models show a shallow silicate absorption feature ($\tau_{10\,\mu m}^{\rm app} = 0.41$) from which we derived an optical extinction of $A_V^{\rm app} = 11$ mag. As for most of the galaxies in the sample, we find $N_H^{\rm LOS} < N_H^{\rm X-rays}$, indicating that the X-ray obscuring region must be closer to the central engine than the torus material.

NGC 1808. The Sy2 galaxy NGC 1808 is undergoing an intense episode of star formation in its central 750 pc (Tacconi-Garman et al. 1996, 2005; Galliano & Alloin 2008). The near-IR fluxes were obtained using ISAAC/VLT, and we measured the mid-IR flux from 10.7 and 18.2 μm OSCIR/CTIO images. Consequently, NGC 1808 has relatively low spatial resolution for our sample (the angular resolution of the ISAAC images is $\sim$0″.6 and that of the OSCIR image at CTIO is $\sim$0″.9–1″). The near-IR SED shape is flat and peculiar, and star formation may contaminate these measurements (according to the argument of Section 5.2), making the fit not very reliable. Low values of σ and i are preferred ($<35°$ and $37°\pm^{19}_{23}$, respectively), contrary to the general trend for the Sy2 galaxies in our sample. The median value of the number of clouds is $N_0 = 8\pm^5_4$, the optical depth per cloud $\tau_V > 122$, and $q = 1.2 \pm 0.9$. The calculated optical extinction produced by the torus is $A_V^{\rm LOS} < 140$ mag. From the bolometric luminosities derived from the fit, we derive the reprocessing efficiency of the modeled torus that results on $\sim$45%. The 10 μm silicate feature appears in weak emission in the fitted spectrum ($\tau_{10\,\mu m}^{\rm app} = -0.21$). Summarizing, due to the intense stellar formation that is taking place in the nuclear region of this galaxy, and to the lower spatial resolution near- and mid-IR measurements that we have for it (all from 3 or 4 m telescopes), the IR SED of NGC 1808 is very likely contaminated with starlight. This is probably producing its peculiar shape and the different trends in the fitted parameters, in comparison with the rest of Sy2 in the sample. For these reasons, we consider the NGC 1808 SED fit unreliable.

NGC 3081. NGC 3081 is a Sy2 galaxy with intense stellar formation located in a series of nested ringlike features (Buta et al. 2004). As in the case of NGC 1386, the SED of NGC 3081 is formed with only three data points, and the model results are similar, with the probability distributions of the parameters presenting the same shapes. The N_0 and τ_V histograms have median values of $N_0 = 10 \pm 3$ and $\tau_V = 47\pm^{42}_{23}$, respectively. We determine lower limits of $\sigma > 52°$, $q > 1.2$, and $i > 42°$. $A_V^{\rm LOS}$ is estimated to be lower than 450 mag. According to the calculated luminosities for this galaxy, the fraction of reprocessed radiation ($L_{\rm bol}^{\rm tor}/L_{\rm bol}^{\rm AGN}$) is among the highest in the sample ($\sim$90%). The 10 μm silicate feature is reproduced in absorption by the models ($\tau_{10\,\mu m}^{\rm app} = 0.91$), from which we inferred an optical obscuration $A_V^{\rm app} \sim 23$ mag.

NGC 3281. This Sy2 galaxy suffers large extinction ($A_V = 22\pm11$ mag to the IR-emitting and $N_H = 2\times10^{24}$ cm^{-2} to the X-ray-emitting regions; Simpson 1998; Vignali & Comastri 2002). The clumpy models fit the data well, except for the 18.3 μm point, which the models underestimate slightly. The probability distributions resulting from the fit show that large values of σ and i are more probable than others ($>68°$ and $>49°$, respectively) and establish an upper limit for the optical depth per cloud of $\tau_V < 12$ at a 68% confidence level. The number of clumps N_0 presents a Gaussian distribution with a tail toward large values, with median value $N_0 = 6\pm^4_2$, as the q histogram (median value

of $q = 1.3\pm^{1.1}_{0.8}$). The optical extinction produced by the clumpy torus corresponds to a Gaussian distribution of median value $A_V^{\rm LOS} = 55\pm^{18}_{15}$ mag. The models predict the 10 μm silicate feature in shallow absorption ($\tau_{10\,\mu m}^{\rm app} = 0.21$), resulting in an apparent optical obscuration of $A_V^{\rm app} = 5$ mag. $N_H^{\rm LOS} < N_H^{\rm X-rays}$, indicating a closer X-ray obscuring region to the central engine than the torus material.

NGC 4388. This highly inclined disk galaxy is spectroscopically classified as a Sy2 nucleus (Phillips & Malin 1982). However, Shields et al. (1996) report the detection of weak, broad Hα emission. The ground-based L-band point introduces a bump in the SED around 3–4 μm, which likely represents starlight contamination (Section 5.2). Indeed, the galaxy appears very extended in the L band (Alonso-Herrero et al. 2003), making difficult to isolate the nuclear emission. Thus, the fit correctly reproduces the near-IR and the N-band points but severely underestimates the Q-band measurement. The probability distributions establish lower limits of $\sigma > 53°$ and $i > 38°$, and upper limits of $q < 1.6$ and $\tau_V < 14$ at a 68% confidence level. The median value of the number of clouds is $N_0 = 9\pm^4_3$. Along the line of sight, $A_V < 80$ mag. The silicate feature appears in shallow absorption in the fitted models ($\tau_{10\,\mu m}^{\rm app} = 0.51$), allowing us to estimate an optical obscuration of $A_V^{\rm app} = 13$ mag. As for most of the galaxies in the sample, we found $N_H^{\rm LOS} < N_H^{\rm X-rays}$.

NGC 7172. NGC 7172 is a Type-2 Seyfert nucleus in a nearly edge-on spiral galaxy. A prominent dust lane in the east–west direction crosses the galaxy. Similar to the case of NGC 4388, we observe a near-IR bump of emission in the SED of NGC 7172, which stellar contamination of the seeing-limited fluxes likely produces (Section 5.2). The N_0 histogram shows a Gaussian shape, with median value $N_0 = 5\pm^3_1$. High values of i, σ, and q are more probable ($i > 45°$, $\sigma > 54°$, and $q > 1.7$, respectively), while low values of τ_V are preferred ($\tau_V < 12$). The torus produces optical extinction $A_V^{\rm LOS} = 50 \pm 20$ mag. The reprocessing efficiency of this galaxy is high ($\sim$80%), according to the derived values of the AGN and torus bolometric luminosities. T-ReCS mid-IR spectroscopy shows a substantial silicate absorption feature (Roche et al. 2007) that is not reproduced by the fitted models, that predict it in very extremely emission (and self-absorbed). This could be due to the above-mentioned stellar contamination of the near-IR fluxes, that in addition to the lack of Q-band data point for this galaxy, make it difficult the correct reproduction of the silicate feature in absorption.

NGC 7582. NGC 7582 is a Sy2 galaxy that harbors a nuclear starburst surrounding the active nucleus (Cid Fernandes et al. 2001; Sosa-Brito et al. 2001; Wold & Galliano 2006; Bianchi et al. 2007) and presents a nuclear outflow (Morris et al. 1985). The fit with the clumpy models shown in Figure 7 does not reproduce the 18.2 μm point, and the resulting probability distributions of the parameters are very different compared with the rest of Sy2 galaxies discussed here (except for NGC 1808). Low values of σ are more probable ($<29°$), as are extremely small numbers of clouds ($N_0 < 2$). High values of q (>2.5) and low values of the τ_V (<27) are preferred. The i probability distribution has a Gaussian shape whose median value is $i = 41°\pm^{19}_{28}$. The optical obscuration produced by the torus results in an unrealistic value of $A_V^{\rm LOS} < 6$ mag. The reprocessing efficiency fraction of this galaxy is among the lowest in the sample ($\sim$10%), a consequence of the low values of N_0 and σ. The 10 μm silicate feature appears in emission

in the fitted models, in contradiction with TIMMI2 mid-IR observations (Siebenmorgen et al. 2004a) that show a strong absorption band characterized by $\tau_{10\,\mu m} = 1.1$. All these results are probably due to stellar contamination of our mid-IR data (obtained at the 4 m CTIO). The intense circumnuclear star formation present in this galaxy makes it more difficult to isolate the torus emission from that of the host galaxy. Consequently, as for the case of NGC 1808, we consider the model fit of NGC 7582 unreliable.

NGC 1365. This Sy1.8 nucleus is hosted in a galaxy with intense nuclear star formation. The X-ray emission of NGC 1365 is also remarkable, showing the most dramatic spectral changes observed in an AGN (Risaliti et al. 2005, 2007). The rapid X-ray variability is attributable to variations in the LOS density, which is compatible with a low number of clouds along the LOS. The clumpy models fit the SED of NGC 1365 well, but the model parameters are not well constrained. The number of clouds has a median value of $7\pm_4^5$ (which is consistent with the rapid X-ray variability), $\sigma = 35°\pm_{13}^{20}$, and $\tau_V = 111\pm_{56}^{58}$. Low values of q and i ($q < 1.7$ and $i < 42°$) are more probable. The optical obscuration due to the torus is $A_V^{LOS} < 170$ mag. The silicate feature is completely absent in the fitted models.

NGC 2992. This galaxy is optically classified as a Sy1.9 nucleus, based on early published spectra (Ward et al. 1980), which showed a weak broad Hα component, but no broad Hβ. In a later observation (Allen et al. 1999), the broad component of Hα disappeared, leading to a new classification of the galaxy as a Sy2. Gilli et al. (2000) reported that the spectrum regained the broad wings of Hα coinciding with a period of intense X-ray activity, contrary to the low stage that was taking place during Allen's observations. Trippe et al. (2008) report the re-classification of NGC 2992 as a Sy2 nucleus again, as of 2006. The near-IR ground-based data were taken in 1998 April, coinciding with the epoch of Gilli's observations, and thus with the classification as intermediate-type Seyfert. On the other hand, our mid-IR measurements from Michelle were obtained in 2006 May, coinciding with the Sy2 state. Thus, our IR SED includes fluxes taken during different periods of activity of NGC 2992. This can explain its similarity with a typical Sy2 SED. The clumpy models that include only torus emission (and no direct AGN component) fit the observed data well. The probability distributions are Gaussians for σ, N_0, and τ_V, with median values $\sigma = 45°\pm_{21}^{18}$, $N_0 = 7\pm_3^5$, and $\tau_V = 36\pm_{11}^{14}$. High values of i ($>53°$) and low values of q (<1.0) are preferred. The calculated optical extinction due to the torus is $A_V < 160$ mag. NGC 2992 is the only intermediate-type Seyfert with the 10 μm silicate feature in absorption in the fitted models ($\tau_{10\,\mu m}^{app} = 0.74$). The derived apparent optical extinction from the measurement of the band is $A_V^{app} \sim 19$ mag. The hydrogen column density along the LOS results in $N_H^{LOS} = 2.5 \times 10^{23}$ cm^{-2}. This value results unrealistic when compared with that inferred from X-ray measurements ($N_H^{X-rays} = 8 \times 10^{21}$ cm^{-2}). This could be due to the intrinsic X-ray variability observed in NGC 2992 (Trippe et al. 2008).

NGC 5506. The nucleus of this galaxy is classified as a Sy1.9 based on the detection of broad wings of the Paβ profile in the near-IR (Blanco et al. 1990). However, more recently, Nagar et al. (2002) presented evidence that NGC 5506 is an obscured narrow-line Sy1, as a result of the finding of the permitted O I $\lambda 1.129$ μm line, together with a broad pedestal of Paβ and rapid X-ray variability. The clumpy models reproduce the near-IR and the N-band data points well, while slightly underestimating the Q-band flux. The discrepancy between the spectral observations

and the model fit along with the poor mid-IR fit together suggest either that additional emission contaminates the near-IR measurements or that the models cannot produce this observed SED shape (Section 5.2). Based on the detection of a water vapor megamaser (Raluy et al. 1998), we have introduced the inclination angle to the code as a Gaussian-prior centered in 85° with a width of 2°. In the resulting probability distributions, we find $\sigma = 25°\pm_7^9$, $q = 2.5\pm_{0.4}^{0.3}$, and the average number of clouds along an equatorial ray to be less than 2. The optical depth per cloud $\tau_V < 68$, and the calculated torus optical extinction is $A_V < 90$ mag. NGC 5506 has the highest L_{bol}^{AGN} of the sample (7.3×10^{44} erg s^{-1}; Table 9). As a consequence of the low values of N_0 and σ derived from its fit, the reprocessing efficiency is low (7%). The galaxy nucleus is very compact in the mid-IR, with an apparent optical depth of $\tau_{10\,\mu m}^{app} \sim 1.4$ (Roche et al. 1991, 2007; Siebenmorgen et al. 2004b), although NGC 5506 also shows variations in its silicate absorption depth on parsec scales (Roche et al. 2007). Unfortunately, the fitted models reproduce the silicate feature in emission ($\tau_{10\,\mu m}^{app} = -0.21$), contrary to the spectroscopic observations. This galaxy has comparable X-ray and mid-IR absorbing columns, indicating that the dust-free absorption in this galaxy is lower than for the Sy2 reported here.

NGC 3227. This active nucleus is usually classified as a Sy1.5. *XMM-Newton* observations show short-term hard X-ray variability likely related to variation in the intrinsic continuum emission (Gondoin et al. 2003). The clumpy models reproduce the SED well, including the direct though extinguished AGN emission (using the Calzetti et al. (2000) law), as in the case of NGC 4151. The resulting histograms show broad Gaussian distributions of the σ, N_0, and τ_V parameters, with median values of $33°\pm_{12}^{20}$, $6\pm_4^5$, and $116\pm_{55}^{56}$, respectively. Low values of i ($<48°$) are more probable than others, and the q parameter results unconstrained. The optical depth calculated using the fitted model parameters is $A_V^{LOS} < 210$ mag. On the other hand, the extinction that obscures the direct AGN emission is $A_V = 2.7\pm_{1.5}^{2.0}$ mag (not related with the torus). This value is intermediate among those reported in the literature of $A_V = 1.2$–1.7 mag (Cohen 1983; González-Delgado & Pérez 1997) and $A_V = 4.5$–4.9 mag (Mundell et al. 1995). The 10 μm silicate feature is practically absent from the fitted models ($\tau_{10\,\mu m}^{app} = -0.1$).

NGC 4151. The nucleus of this well-known Sy1.5 galaxy shows flux variability in a wide wavelength range, with timescales ranging from a few hours in the hard X-rays (Yaqoob et al. 1993) to several months in the IR (Oknyanskij et al. 1999). Shapovalova et al. (2008) reported changes in the spectral type of the nucleus from a Sy1.5 to a Sy1.8, coinciding with maximum and minimum activity states, respectively. The SED of NGC 4151 is one of the flattest in our sample, with the near-IR excess likely due to direct AGN emission, which is absent in the Sy2 galaxies. We include this power-law contribution and allow for some extinction to account for the observed reddening of the active nucleus. The fit correctly reproduces the observed SED, especially in the near-IR. The probability distributions establish a median value of $q = 1.7\pm_{0.9}^{0.8}$, $i = 41°\pm_{28}^{23}$, and $\tau_V = 120\pm_{48}^{55}$. Low values for the number of clouds along equatorial rays ($N_0 < 3$) and for the width of the angular distribution ($\sigma < 32°$) are more probable. The optical extinction derived from the fitted model parameters is $A_V^{LOS} < 65$ mag. On the other hand, the optical obscuration of the direct AGN emission (not produced by the torus) is another free parameter of the fit, and we find $A_V = 2.5\pm_{1.6}^{1.4}$ mag. The 10 μm silicate feature

appears in weak emission ($\tau_{10\,\mu m}^{app} = -0.31$) in the fitted models, in qualitative agreement with *Spitzer* observations of this galaxy (Weedman et al. 2005).

REFERENCES

Allen, M. G., Dopita, M. A., Tsvetanov, Z. I., & Sutherland, R. S. 1999, ApJ, 511, 686
Alonso-Herrero, A., Quillen, A. C., Rieke, G. H., Ivanov, V. D., & Efstathiou, A. 2003, AJ, 126, 81
Alonso-Herrero, A., Quillen, A. C., Simpson, C., Efstathiou, A., & Ward, M. J. 2001, AJ, 121, 1369
Alonso-Herrero, A., Ward, M. J., & Kotilainen, J. K. 1996, MNRAS, 278, 902
Antonucci, R. R. J. 1993, ARA&A, 31, 473
Asensio Ramos, A., & Ramos Almeida, C. 2009, ApJ, 696, 2075
Awaki, H., Murakami, H., Ogawa, Y., & Leighly, K. M. 2006, ApJ, 645, 928
Bailey, J., Sparks, W. B., Hough, J. H., & Axon, D. J. 1986, Nature, 322, 150
Ballantyne, D. R., Shi, Y., Rieke, G. H., Donley, J. L., Papovich, C., & Rigby, J. R. 2006, ApJ, 653, 1070
Barmby, P., et al. 2006, ApJ, 642, 126
Barvainis, R. 1987, ApJ, 320, 537
Beckmann, V., Shrader, C. R., Gehrels, N., Soldi, S., Lubiński, P., Zdziarski, A. A., Petrucci, P.-O., & Malzac, J. 2005, ApJ, 634, 939
Bennert, N., Jungwiert, B., Komossa, S., Haas, M., & Chini, R. 2006, A&A, 446, 919
Bianchi, S., Chiaberge, M., Piconcelli, E., & Guainazzi, M. 2007, MNRAS, 374, 697
Blanco, P. R., Ward, M. J., & Wright, G. S. 1990, MNRAS, 242, 4
Bohlin, R. C., Savage, B. D., & Drake, J. F. 1978, ApJ, 224, 132
Braatz, J., Greenhill, L., Moran, J., Wilson, A., & Herrnstein, J. 1997, BAAS, 29, 1374
Buta, R. J., Byrd, G. G., & Freeman, T. 2004, AJ, 127, 1982
Calzetti, D., et al. 2000, ApJ, 533, 682
Carollo, C. M., Stiavelli, M., Seigar, M., de Zeeuw, P. T., & Dejonghe, H. 2002, AJ, 123, 159
Chiaberge, M., Capetti, A., & Celotti, A. 2001, MNRAS, 324, L33
Cid Fernandes, R., Heckman, T., Schmitt, H., Delgado, R. M. G., & Storchi-Bergmann, T. 2001, ApJ, 558, 81
Cohen, R. D. 1983, ApJ, 273, 489
Colina, L., Sparks, W. B., & Macchetto, F. 1991, ApJ, 370, 102
Davies, R. I., et al. 2006, ApJ, 646, 754
Dewangan, G. C., & Griffiths, R. E. 2005, ApJ, 625, 31
Dullemond, C. P., & van Bemmel, I. M. 2005, A&A, 436, 47
Edelson, R. A., Malkan, M. A., & Rieke, G. H. 1987, ApJ, 321, 233
Efstathiou, A., & Rowan-Robinson, M. 1995, MNRAS, 273, 649
Elitzur, M., & Shlosman, I. 2006, ApJ, 648, L101
Elvis, M., Risaliti, G., Nicastro, F., Miller, J. M., Fiore, F., & Puccetti, S. 2004, ApJ, 615, L25
Elvis, M., et al. 1994, ApJS, 95, 1
Fadda, D., Giuricin, G., Granato, G. L., & Vecchies, D. 1998, ApJ, 496, 117
Fritz, J., Franceschini, A., & Hatziminaoglou, E. 2006, MNRAS, 366, 767
Galliano, E., & Alloin, D. 2008, A&A, 487, 519
Gilli, R., Maiolino, R., Marconi, A., Risaliti, G., Dadina, M., Weaver, K. A., & Colbert, E. J. M. 2000, A&A, 355, 485
Glasse, A. C., Atad-Ettedgui, E. I., & Harris, J. W. 1997, Proc. SPIE, 2871, 1197
Gondoin, P., Orr, A., Lumb, D., & Siddiqui, H. 2003, A&A, 397, 883
González-Delgado, R. M., & Pérez, E. 1997, MNRAS, 284, 931
Granato, G. L., & Danese, L. 1994, MNRAS, 268, 235
Granato, G. L., Danese, L., & Franceschini, A. 1997, ApJ, 486, 147
Greenhill, L. J., et al. 2003, ApJ, 590, 162
Groves, B., Dopita, M., & Sutherland, R. 2006, A&A, 458, 405
Guainazzi, M., Matt, G., & Perola, G. C. 2005, A&A, 444, 119
Hao, L., Weedman, D. W., Spoon, H. W. W., Marshall, J. A., Levenson, N. A., Elitzur, M., & Houck, J. R. 2007, ApJ, 655, L77
Hao, L., et al. 2005a, AJ, 129, 1795
Hao, L., et al. 2005b, ApJ, 625, L75
Helou, G., et al. 2004, ApJS, 154, 253
Hönig, S. F., Beckert, T., Ohnaka, K., & Weigelt, G. 2006, A&A, 452, 459
Hough, J. H., Bailey, J. A., Rouse, M. F., & Whittet, D. C. B. 1987, MNRAS, 227, 1
Ivezić, Ž., Nenkova, M., & Elitzur, M. 1999, User Manual for DUSTY Univ. of Kentucky Internal Report (arXiv:astro-ph/9910475)
Jaffe, W., et al. 2004, Nature, 429, 47

Jiménez-Bailón, E., Santos-Lleó, M., Dahlem, M., Ehle, M., Mas-Hesse, J. M., Guainazzi, M., Heckman, T. M., & Weaver, K. A. 2005, A&A, 442, 861
Kotilainen, J. K., Ward, M. J., Boisson, C., Depoy, D. L., Smith, M. G., & Bryant, L. R. 1992, MNRAS, 256, 125
Krolik, J. H., & Begelman, M. C. 1988, ApJ, 329, 702
Kuraszkiewicz, J. K., et al. 2003, ApJ, 590, 128
Lamer, G., Uttley, P., & McHardy, I. M. 2000, MNRAS, 319, 949
Lamer, G., Uttley, P., & McHardy, I. M. 2003, MNRAS, 342, L41
Levenson, N. A., Heckman, T. M., Krolik, J. H., Weaver, K. A., & Życki, P. T. 2006, ApJ, 648, 111
Levenson, N. A., Sirocky, M. M., Hao, L., Spoon, H. W. W., Marshall, J. A., Elitzur, M., & Houck, J. R. 2007, ApJ, 654, L45
Marconi, A., Schreier, E. J., Koekemoer, A., Capetti, A., Axon, D., Macchetto, D., & Caon, N. 2000, ApJ, 528, 276
Markowitz, A., et al. 2007, ApJ, 665, 209
Martini, P., & Pogge, R. W. 1999, AJ, 118, 2646
Mason, R. E., Geballe, T. R., Packham, C., Levenson, N. A., Elitzur, M., Fisher, R. S., & Perlman, E. 2006, ApJ, 640, 612
Mason, R. E., Levenson, N. A., Packham, C., Elitzur, M., Radomski, J., Petric, A. O., & Wright, G. S. 2007, ApJ, 659, 241
Mason, R. E., Levenson, N. A., Shi, Y., Packham, C., Gorjian, V., Cleary, K., Rhee, J., & Werner, M. 2009, ApJ, 693, L136
Mauder, W., et al. 1992, A&A, 264, 9
Meisenheimer, K., et al. 2007, A&A, 471, 453
Morris, S., Ward, M., Whittle, M., Wilson, A. S., & Taylor, K. 1985, MNRAS, 216, 193
Mundell, C. G., Holloway, A. J., Pedlar, A., Meaburn, J., Kukula, M. J., & Axon, D. J. 1995, MNRAS, 275, 67
Nagar, N. M., Oliva, E., Marconi, A., & Maiolino, R. 2002, A&A, 391, L21
Nagar, N. M., Wilson, A. S., Mulchaey, J. S., & Gallimore, J. F. 1999, ApJS, 120, 209
Nenkova, M., Ivezić, Ž., & Elitzur, M. 2002, ApJ, 570, 9
Nenkova, M., Sirocky, M. M., Ivezić, Ž., & Elitzur, M. 2008a, ApJ, 685, 147
Nenkova, M., Sirocky, M. M., Nikutta, R., Ivezić, Ž., & Elitzur, M. 2008b, ApJ, 685, 160
Netzer, H., et al. 2007, ApJ, 666, 806
Oknyanskij, V. L., Lyuty, V. M., Taranova, O. G., & Shenavrin, V. I. 1999, Astron. Lett., 25, 483
Ossenkopf, V., Henning, Th., & Mathis, J. S. 1992, A&A, 261, 567
Osterbrock, D. E. 1981, ApJ, 249, 462
Packham, C., Hough, J. H., Young, S., Chrysostomou, A., Bailey, J. A., Axon, D. J., & Ward, M. J. 1996, MNRAS, 278, 406
Packham, C., Radomski, J. T., Roche, P. F., Aitken, D. K., Perlman, E., Alonso-Herrero, A., Colina, L., & Telesco, C. M. 2005, ApJ, 618, L17
Phillips, M. M., & Malin, D. F. 1982, MNRAS, 199, 905
Pier, E. A., & Krolik, J. H. 1992, ApJ, 401, 99
Pier, E. A., & Krolik, J. H. 1993, ApJ, 418, 673
Polletta, M., Bassani, L., Malaguti, G., Palumbo, G. G. C., & Caroli, E. 1996, ApJS, 106, 399
Polletta, M., et al. 2007, ApJ, 663, 81
Prieto, M. A., Reunanen, J., & Kotilainen, J. K. 2002, ApJ, 571, L7
Prieto, M. A., et al. 2004, ApJ, 614, 135
Ptak, A., & Griffiths, R. 2003, in ASP Conf. Ser. 295, Astronomical Data Analysis Software and Systems XII, ed. H. E. Payne, R. I. Jedrzejewski, & R. N. Hook (San Francisco, CA: ASP), 465
Quillen, A. C., McDonald, C., Alonso-Herrero, A., Lee, A., Shaked, S., Rieke, M. J., & Rieke, G. H. 2001, ApJ, 547, 129
Raban, D., Jaffe, W., Röttgering, H., Meisenheimer, K., & Tristram, K. 2009, MNRAS, 394, 1325
Radomski, J. T., Piña, R. K., Packham, C., Telesco, C. M., De Buizer, J. M., Fisher, R. S., & Robinson, A. 2003, ApJ, 587, 117
Radomski, J. T., Piña, R. K., Packham, C., Telesco, C. M., & Tadhunter, C. N. 2002, ApJ, 566, 675
Radomski, J. T., et al. 2008, ApJ, 681, 141
Raluy, F., Planesas, P., & Colina, L. 1998, A&A, 335, 113
Ramos Almeida, C., Pérez García, A. M., Acosta-Pulido, J. A., & González-Martín, O. 2008, ApJ, 680, L17
Ramos Almeida, C., Pérez García, A. M., Acosta-Pulido, J. A., & Rodríguez Espinosa, J. M. 2007, AJ, 134, 2006
Ramos Almeida, C., Rodríguez Espinosa, J. M., Barro, G., Gallego, J., & Pérez-González, P. G. 2009, AJ, 137, 179
Rieke, G. H. 1978, ApJ, 226, 550
Rieke, G. H., & Lebofsky, M. J. 1981, ApJ, 250, 87
Rigby, J. R., et al. 2004, ApJS, 154, 160
Risaliti, G., Elvis, M., Fabbiano, G., Baldi, A., & Zezas, A. 2005, ApJ, 623, 93
Risaliti, G., Elvis, M., Fabbiano, G., Baldi, A., Zezas, A., & Salvati, M. 2007, ApJ, 659, L111

Roche, P. F., Aitken, D. K., Smith, C. H., & Ward, M. J. 1991, MNRAS, 248, 606

Roche, P. F., Packham, C., Aitken, D. K., & Mason, R. E. 2007, MNRAS, 375, 99

Roche, P. F., Packham, C., Telesco, C. M., Radomski, J. T., Alonso-Herrero, A., Aitken, D. K., Colina, L., & Perlman, E. 2006, MNRAS, 367, 1689

Sanders, D. B., Phinney, E. S., Neugebauer, G., Soifer, B. T., & Matthews, K. 1989, ApJ, 347, 29

Schartmann, M., Meisenheimer, K., Camenzind, M., Wolf, S., Tristram, K. R. W., & Henning, T. 2008, A&A, 482, 67

Schmitt, H. R., Antonucci, R. R. J., Ulvestad, J. S., Kinney, A. L., Clarke, C. J., & Pringle, J. E. 2001, ApJ, 555, 663

Schreier, E. J., et al. 1998, ApJ, 499, L143

Shapovalova, A. I., et al. 2008, A&A, 486, 99

Shields, J. C., & Filippenko, A. V. 1996, A&A, 311, 393

Shu, X. W., Wang, J. X., Jiang, P., Fan, L. L., & Wang, T. G. 2007, ApJ, 657, 167

Siebenmorgen, R., Haas, M., Krügel, E., & Schulz, B. 2005, A&A, 436, L5

Siebenmorgen, R., Krügel, E., & Spoon, H. W. W. 2004a, A&A, 414, 123

Siebenmorgen, R., Krügel, E., & Spoon, H. W. W. 2004b, A&A, 419, 49

Silbermann, N. A., et al. 1999, ApJ, 515, 1

Simpson, C. 1998, ApJ, 509, 653

Simpson, C., Ward, M., & Kotilainen, J. 1994, MNRAS, 271, 250

Sirocky, M. M., Levenson, N. A., Elitzur, M., Spoon, H. W. W., & Armus, L. 2008, ApJ, 678, 729

Soifer, B. T., Bock, J. J., Marsh, K., Neugebauer, G., Matthews, K., Egami, E., & Armus, L. 2003, AJ, 126, 143

Soldi, S., et al. 2005, A&A, 444, 431

Sosa-Brito, R. M., Tacconi-Garman, L. E., Lehnert, M. D., & Gallimore, J. F. 2001, ApJS, 136, 61

Spinoglio, L., & Malkan, M. A. 1989, ApJ, 342, 83

Sturm, E., et al. 2005, ApJ, 629, L21

Tacconi-Garman, L. E., Sternberg, A., & Eckart, A. 1996, AJ, 112, 918

Tacconi-Garman, L. E., et al. 2005, A&A, 432, 91

Telesco, C. M., Piña, R. K., Hanna, K. T., Julian, J. A., Hon, D. B., & Kisko, T. M. 1998, Proc. SPIE, 3354, 534

Tozzi, P., et al. 2001, ApJ, 562, 42

Treister, E., et al. 2004, ApJ, 616, 123

Trippe, M. L., Crenshaw, D. M., Deo, R., & Dietrich, M. 2008, AJ, 135, 2048

Tristram, K. R. W., et al. 2007, A&A, 474, 837

Tsvetanov, Z., & Walsh, J. R. 1992, ApJ, 386, 485

Turner, P. C., Forrest, W. J., Pipher, J. L., & Shure, M. A. 1992, ApJ, 393, 648

Turner, T. J., George, I. M., Nandra, K., & Mushotzky, R. F. 1997, ApJS, 113, 23

Turner, T. J., Perola, G. C., Fiore, F., Matt, G., George, I. M., Piro, L., & Bassani, L. 2000, ApJ, 531, 245

Urry, C. M., & Padovani, P. 1995, PASP, 107, 803

Vignali, C., & Comastri, A. 2002, A&A, 381, 834

Ward, M., Elvis, M., Fabbiano, G., Carleton, N. P., Willner, S. P., & Lawrence, A. 1987, ApJ, 315, 74

Ward, M., Penston, M. V., Blades, J. C., & Turtle, A. J. 1980, MNRAS, 193, 563

Weedman, D. W., et al. 2005, ApJ, 633, 706

Wilson, A. S., Shopbell, P. L., Simpson, C., Storchi-Bergmann, T., Barbosa, F. K. B., & Ward, M. J. 2000, AJ, 120, 1325

Wold, M., & Galliano, E. 2006, MNRAS, 369, 47

Yaqoob, T., et al. 1993, MNRAS, 262, 435

Yaqoob, T., et al. 2007, PASJ, 59, 283

Young, S., Packham, C., Mason, R. E., Radomski, J. T., & Telesco, C. M. 2007, MNRAS, 378, 888